Research Square

Preprints are preliminary reports that have not undergone peer review.
They should not be considered conclusive, used to inform clinical practice,
or referenced by the media as validated information.

# In situ architecture of PML nuclear bodies reveals a porous, chromatin-permissive interior

**Stephen Carter**

stephen.carter@glasgow.ac.uk

MRC-University of Glasgow Centre for Virus Research https://orcid.org/0000-0003-4698-7552

**Vojtěch Pražák**

Centre for Structural Systems Biology https://orcid.org/0000-0001-8149-218X

**Iain Harley**

Centre for Virus Research https://orcid.org/0000-0002-3767-4450

**Julian Falckenhayn**

Centre for Structural Systems Biology

**Peter Thomason**

Cancer Research UK Scotand Institute

**Chris Boutell**

Centre for Virus Research https://orcid.org/0000-0002-2970-7785

**Benjamin Davis**

Department of Pharmacology https://orcid.org/0000-0002-5056-407X

**Rainer Kaufmann**

University of Hamburg https://orcid.org/0000-0002-4165-0195

**Article**

**Keywords:**

**Posted Date:** November 25th, 2026

**DOI:** https://doi.org/10.21203/rs.3.rs-11537093/v1

**License:** This work is licensed under a Creative Commons Attribution 4.0 International License.
Read Full License

**Additional Declarations:** There is **NO** Competing Interest.

# *In situ* architecture of PML nuclear bodies reveals a porous, chromatin-permissive interior

Vojtěch Pražák[1,2], Iain Harley[3,4], Julian Falckenhayn[1,5], Chris Boutell[3], Peter A. Thomason[4], Benjamin G. Davis[6,7,8], Rainer Kaufmann[1,5], Stephen D. Carter[3,4 *]

1Centre for Structural Systems Biology, Notkestraße 85, c/o DESY, Geb. 15, 22607 Hamburg, Germany. 2Department of Biochemistry, University of Oxford, South Parks Road, Oxford OX1 3QU, United Kingdom. 3MRC-University of Glasgow Centre for Virus Research, School of Infection & Immunity, Glasgow G61 1QH, United Kingdom. 4Cancer Research UK Scotland Institute, Glasgow, G61 1QH, United Kingdom. 5Department of Physics, University of Hamburg, Notkestraße 9-11, 22607 Hamburg, Germany. 6The Rosalind Franklin Institute, Didcot OX11 0QX, United Kingdom. 7Department of Chemistry, Chemistry Research Laboratory, University of Oxford, Oxford OX1 3TA, United Kingdom. 8Department of Pharmacology, University of Oxford, Oxford OX1 3QT, United Kingdom. *To whom correspondence should be addressed (stephen.carter@glasgow.ac.uk).

## Abstract

Membrane-less nuclear compartments are usually defined by the proteins and nucleic acids they concentrate, yet how their interiors select content is unclear. Promyelocytic leukemia (PML) bodies are hubs for telomere maintenance and the DNA damage response whose interior has never been resolved *in situ*. Using a cryogenic correlative light and electron microscopy pipeline with super-resolution localisation and cryo-electron tomography, we imaged eYFP-PML-I bodies as a diffuse PML-protein shell enclosing a core built from a fibrous network denser than the surrounding nucleoplasm. Template matching and subtomogram averaging mapped TRiC chaperonin in closed and open conformations and single-capped PA28 proteasomes, and revealed ordered columnar trinucleosome assemblies. Visual proteomics placed chromatin inside the body at nucleoplasmic density, whereas TRiC chaperonins and PA28-capped proteasomes were depleted. The interior is therefore a porous meshwork that holds chromatin but restricts larger soluble complexes, consistent with content selection by size-dependent partitioning.

The eukaryotic nucleus achieves its spatial organisation through selective separation, generating membrane-less condensates. Some of these, including nucleoli, nuclear speckles, paraspeckles and classical Cajal bodies[1,2], assemble through multivalent protein-protein and protein-RNA interactions, often involving the intrinsically disordered regions (IDRs) of RNA-binding proteins. Insights into the resulting specialised biochemical environments have given insight into the way that they regulate nuclear processes[3]. By contrast, other important nuclear bodies are much less characterised; foremost amongst these are the promyelocytic leukemia (PML) bodies that assemble through exploitation of SUMO (small ubiquitin-like modifier)–SIM (SUMO-interacting motif) networks, forming major hubs that can concentrate hundreds of client proteins[4,5]. Functionally, PML bodies orchestrate telomere maintenance, cellular senescence, protein degradation, the DNA damage response, gene

transcription, apoptosis and antiviral defence[6,7] yet the underlying mechanisms and, indeed, the structure that accomplishes this remains opaque.

PML bodies were first observed by conventional electron microscopy in the 1960s as electron-dense interchromatin nuclear bodies[8,9]. These structures gained molecular identity when cloning of PML from the acute promyelocytic leukemia (APL) translocation[10,11] was followed by immuno-labelling electron microscopy studies demonstrating that PML protein localized specifically to these nuclear bodies[12,13]. The observation that these bodies were disrupted in APL and reformed upon treatment has provided an archetypal example of targeted cancer therapy[14].

The characteristic PML body architecture comprises a ~100 nm PML-containing shell surrounding a PML-free inner core[15,16]. Super-resolution microscopy, particularly 4Pi fluorescence imaging[17], suggests that PML and Sp100 proteins form distinct, partially overlapping patches within this shell, potentially enabling dynamic protein exchange with the nucleoplasm[18]. This ring-like shell architecture has also been shown by 3D-SIM[19]. One central PML protein, TRIM19, belongs to the tripartite motif (TRIM) family characterised by an N-terminal RING domain, two B-box zinc finger domains, and a coiled-coil region. This architecture resembles that of TRIM5α, which restricts retroviral infection and contains only a single B-box domain[20].

While PML body cores are generally considered protein-rich structures, DNA incorporation into specialised subtypes has also been reported. Alternative lengthening of telomeres (ALT)-associated PML bodies (APBs) in telomerase-negative cancer cells contain telomeric DNA that supports recombination-based telomere maintenance[21,22], while satellite DNA accumulates in PML bodies during G2 to promote heterochromatin remodelling[23]. Giant PML bodies in ICF (immunodeficiency, centromeric instability and facial anomalies) syndrome contain under-condensed satellite DNA cores[23], and latent herpesvirus genomes are sequestered within viral PML bodies as a seeming antiviral mechanism[24–26]. Together, these observations suggest that DNA content of PML bodies may be dynamic and functionally regulated. Notably, although PML bodies have been suggested to associate with chromatin[16,18,27], direct evidence such as through visualisation of nucleosomes within their cores has not been obtained. Conventional imaging approaches lack the resolution to determine the precise organisation of DNA within these condensates. Moreover, any higher-order chromatin architecture of possible telomeric DNA associated with PML bodies remains equally unresolved.

Large protein complexes have also been placed at PML bodies. For example, the nuclear proteasome activator PA28γ binds PML and accumulates in PML bodies, where it regulates their number[28], and

PA28-capped proteasomes are recruited to bodies after interferon γ or arsenic treatment[15,29], but where such complexes sit relative to the body interior is unknown. More broadly, the extent to which macromolecular complexes are selectively partitioned into or excluded from PML body interiors has not been examined at the structural level, leaving a gap in our understanding of the mechanism that underpins their dynamic roles within the nucleus as regulatory hubs.

Here, we show that a cryogenic correlative light and electron microscopy (cryo-CLEM) pipeline using plasma focused ion beam (pFIB) milling can visualise PML bodies at molecular resolution within vitrified nuclei. Using cryo-electron tomography (cryo-ET), template matching and sub-tomogram averaging (STA), this now reveals, by direct visualisation, DNA in nucleosomes including open-state columnar trinucleosome assemblies. This previously unknown chromatin organisation within PML body interiors is accompanied by depletion of large proteasome complexes relative to the volume the body occupies. The pattern is consistent with size-dependent partitioning of soluble macromolecular complexes through a porous interior mesh.

## Results

### Cryo-CLEM and associated textural differences enable efficient identification of PML bodies within nuclei

To characterise the molecular architecture of PML bodies, we employed human foreskin fibroblasts (HFFs) stably expressing doxycycline-inducible eYFP-PML-I[30,31]. HFFs exhibited exceptional thin morphology when cultured on EM grids, making them ideal for accessing deep nuclear regions where PML bodies reside. A 7 hour doxycycline induction was sufficient for eYFP-PML-I to incorporate into existing endogenous PML bodies (Fig. 1a), and plunge-frozen cells with bright nuclear foci were selected for lamella preparation by integrated cryo-fluorescence microscopy (cryo-iFLM; see Methods).

The eYFP-PML-I (hereafter PML-I) signal guided lamella positioning (Fig. 1b). About 40% of lamellae retained detectable fluorescence after milling (Fig. 1c), and on these the fluorescence was registered to the electron micrographs to target tilt-series acquisition to PML-I bodies (Fig. 1d,e). Using this approach, we collected tilt-series both directly on PML-I bodies and in adjacent nuclear regions to representatively sample the surrounding nucleoplasm (Extended Data Fig. 1a,b). In total, from 13 vitreous lamellae we acquired 45 tilt-series targeting 27 PML bodies and 18 neighbouring regions, from which 7 PML-I body cryo-tomograms and 9 nucleoplasmic cryo-tomograms were selected for high-resolution analysis (Supplementary Tables 1 and 2).

The visualisation of membrane-less compartments within cells including inside the nucleus remains comparatively challenging, as they lack clear boundaries and are not evident in electron micrographs without a fluorescence reference (Extended Data Fig. 1b). Advantageously, in our cryo-tomograms, it proved possible to identify PML-I bodies due to an identifiable difference in texture compared to the surrounding nucleoplasm. Assignment of these 400-800 nm diameter structures was provided by the cryo-iFLM signal initially used for targeting regions for high-resolution data acquisition (Fig. 1e,g,h). Further use of IsoNet denoising[32] and total variation denoising[33] revealed a clear, irregularly shaped boundary between the edge of putative PML bodies and granular nucleoplasm (Fig. 1f,i). The interiors contained a fine-grained texture distinct from the larger granular appearance of the surrounding nucleoplasm (Fig. 1f,i), reminiscent of TRIM5α-bodies observed by previous cryo-ET work[34].

**Cryo-SR-CLEM places the PML-I shell at the boundary of the finely textured region**

To precisely co-localise the PML-I shell within these cryo-ET structures, we performed cryogenic super-resolution correlative light and electron microscopy (cryo-SR-CLEM)[35], observing single eYFP-PML-I molecules with an average precision of 7.7 nm (Fig. 1j). Fluorescence signal concentrated at the periphery of these finely textured regions (Fig. 1k,l), thereby placing the eYFP-PML-I shell at their outermost boundary. The boundary is irregularly contoured at the nanoscale, consistent with the uneven boundary visible in cryo-ET between the finely textured body region and the surrounding nucleoplasm. The PML-I protein shell itself, however, is not resolved as a distinct layer in cryo-ET, consistent with the shell being assembled from many small proteins whose densities blend continuously into both the body interior and the surrounding granular nucleoplasm. We also observed membrane vesicles within (n=2) and adjacent to (n=2) PML-I bodies (Fig. 1k,l). For the two vesicles captured by cryo-SR-CLEM, the single-molecule eYFP-PML-I signal did not correlate to membranes, indicating that they do not contain PML-I.

**3D-SIM defines PML-I body dimensions and morphological diversity**

Cryo-ET samples only a few bodies within thin lamellae, so we used 3D-SIM on the same HFF cell line under the same culture conditions to survey PML-I body dimensions and morphology across hundreds of bodies in 16 cells. 3D-SIM confirmed the characteristic hollow shell architecture of PML-I bodies[19] (Fig. 1m,n), but also considerable morphological diversity including classical round bodies, and previously unknown multi-chambered bodies, figure-of-eight configurations, and bodies with internal densities (Fig. 1o–t). Quantitative analysis across 16 cells gave a median diameter of 380 nm and a median outer shell thickness of 105 nm (Fig. 1u–w), consistent with the size of the finely textured regions

that correspond to PML-I bodies in our cryo-tomograms. Interestingly, while 3D-SIM suggests a smooth PML-I protein boundary, cryo-SR-CLEM had revealed this to be unevenly contoured at the nanoscale (Fig. 1k,l).

**PML-I body interiors are distinct from the surrounding nucleoplasm**

To compare the interiors of PML-I bodies with the surrounding nucleoplasm, we delineated each body from the cryo-CLEM signal and the denoised cryo-tomogram by manual segmentation in Amira[36] (Fig. 2a; Supplementary Video 1). Two further fluorescence-positive cryo-tomograms (TS_04 and TS_162) caught less than 10% of a body at the edge of the field of view and were not segmented, leaving five bodies for analysis. The five segmented bodies were similar in size (0.022 to 0.037 μm³ within the lamella) and each was compared with roughly 2.5 to 5.5 times its volume of nucleoplasm.

To assess the distribution of large macromolecular densities, material was detected on every third slice as contiguous dark clusters and binned by size (see Methods; Fig. 2b, Supplementary Fig. 1a to d). High contrast material covered 12 to 18% of the body interior and 17 to 21% of the nucleoplasm (five of five bodies). We found small cluster densities of 6 to 15 nm (yellow in Fig. 2b) were 1.4-fold more abundant inside the body and clusters of 15 to 20 nm (green) were equally abundant. Clusters of 20 to 30 nm (magenta) were 1.6-fold less abundant inside and clusters above 30 nm (dark blue) 4-fold less abundant (per body 1.2 to 2.5 and 2.7 to 15-fold; Fig. 2c).

The area covered by high-contrast material and the density of large clusters both changed as a step within about 50 nm of the cryo-CLEM boundary, from about 15 to 19% and 90 to 170 per μm², respectively (Fig. 2d). Redrawing the boundary 20 nm inside or outside the segmented edge changed the inside to outside ratios by no more than 0.04 (see Methods; Supplementary Fig. 1f). Furthermore, the same pattern was obtained on the raw reconstructions without denoising (Supplementary Fig. 1g). The depletion of large clusters therefore reflects a transition at the body edge rather than the choice of boundary, and indicates that large granular densities are under-represented in PML-I body interiors.

**A denser fibrous network fills the PML-I body interior**

The fine texture of the body interior raised the question of whether it is built from a continuous scaffold, as expected for a compartment assembled by the self-associating coiled coil of PML and as seen in other condensates resolved by cryo-ET[37]. We therefore masked dense clusters of 15 nm and larger and applied skeletonisation[37] and found fibrous networks in both compartments (Fig. 2e).

Inside the body the fibre network covered 4.1 to 5.3% of the area, compared with 2.8 to 3.6% in the nucleoplasm. The interior network was therefore 1.44-fold denser on average, and 1.29 to 1.55-fold in every one of the five bodies. When all dense clusters were masked, the connected strands of the network were 1.6-fold longer inside (43 to 79 nm versus 26 to 43 nm; Supplementary Fig. 1e). This excess fell away at the body boundary, where network density returned to the nucleoplasmic level (Fig. 2f), and was insensitive to redrawing the boundary 20 nm inside or outside the segmented edge (Supplementary Fig. 1f). The PML-I body interior is therefore a distinct compartment. Its boundary is irregular in outline, as cryo-SR-CLEM showed, yet abrupt in texture, as the step in cluster density shows. Moreover, the interior contains a denser fibrous network and fewer large dense clusters than the nucleoplasm around it.

**Vault complexes at the PML-I body periphery**

Among the larger densities at the body periphery, two cryo-tomograms contained intact vault complexes that were recognisable by manual inspection (Fig. 3b–d,q). Immunofluorescence using an antibody against the major vault protein (MVP) revealed discrete puncta adjacent to PML-I bodies in multiple cells (Fig. 3e–g), consistent with these rare events reflecting a genuine spatial association of vault complexes near PML-I bodies. As a positive control, immunofluorescence against Daxx, a known PML body component, showed clear colocalisation with PML-I bodies (Supplementary Fig. 2a–c), confirming the validity of our MVP immunofluorescence approach.

**Molecular architecture within PML-I cryo-tomograms**

Within the fine texture, a wide variety of macromolecular complexes including barrels, granules, filaments, cylindrical structures, elongated barrels and rings could be recognised (Extended Data Fig. 1c–h), as well as densities consistent with nucleosomes. To identify and characterise these macromolecular complexes, we performed template matching[38,39] on 16 cryo-tomograms with thickness between 134 nm and 230 nm. Of these, 7 cryo-tomograms captured eYFP-PML-I fluorescence directly, while 9 captured regions adjacent to PML-I bodies at distances of 780 nm to 4 µm (Supplementary Table 2). Templates were derived from published cryo-EM density maps or atomic models, both templates and cryo-tomograms were low-pass filtered to 40 Å to minimise template bias, and cross-correlation thresholds were selected on the score maps using a custom napari[40] viewer (see Methods; Supplementary Videos 2–8). Selected particle sets were imported into RELION 4.0 for STA with iterative 3D classification; template sources, particle numbers and STA resolutions for all complexes are summarised in Table 1 and Supplementary Table 3.

## TRiC chaperonin complexes form conformation-dependent clusters in the nucleus

Barrel-shaped densities approximately 17 nm in diameter, sometimes in clusters, occurred throughout the cryo-tomograms and matched the double-ring barrel of the TRiC/CCT chaperonin (Extended Data Fig. 1c). To identify them we performed template matching with closed-state and open-state templates (EMDB-18913 and EMDB-18921; Supplementary Videos 2 and 3). Across all 16 cryo-tomograms this gave 335 closed and 413 open TRiC particles, after each position detected by both templates was assigned to the template with the higher cross-correlation (CC) score (Extended Data Fig. 2a,b; see Methods). STA yielded maps of closed TRiC at 22 Å and open TRiC at 32 Å resolution (Fig. 3h–m; Extended Data Fig. 2c–f). Both maps resolved the double-ring barrel with its central cavity. The closed map was compact and symmetric (Fig. 3h–j), whereas the open map displayed splayed apical domains (Fig. 3k–m), and particles of each class mapped back onto densities of the corresponding shape in the cryo-tomograms (Extended Data Fig. 3a–d).

Closed TRiC had a striking tendency to self-associate. DBSCAN clustering[41] of the 3D coordinates (see Methods) placed 29.0% of closed particles (88/303) in 35 clusters (Fig. 3q; Extended Data Fig. 3e,f; Supplementary Videos 1 and 9), but only 5.8% of open particles (16/276) in 8 clusters (Extended Data Fig. 3f), a five-fold difference (Fisher's exact test, $p = 6 \times 10^{-14}$, risk ratio 5.0, 95% CI 3.0–8.3). TRiC self-association is therefore strongly conformation-dependent, as reported for cytoplasmic TRiC by cryo-ET[42], suggesting that clusters mark sites of active protein folding.

Most closed TRiC clusters were dimers (27/35, 77%), with trimers, tetramers, a pentamer and an octamer also present, whereas all open clusters were dimers (8/8; Extended Data Fig. 3f). Paired closed complexes sat 17.3 nm apart (s.d. 0.9 nm, n = 32 pairs), one particle diameter (Extended Data Fig. 3g), and touched head-to-equator (22/32) or equator-to-equator (10/32), with no head-to-head contacts observed (0/32; Extended Data Fig. 3h; see Methods), forming circular (Fig. 3r,s) and linear (Fig. 3t) arrangements. Few TRiC complexes lay inside the segmented PML-I bodies (28 of 194, 14.4%; range 2.6% to 38.3% across cryo-tomograms; Fig. 3a,q; Supplementary Figs. 3 and 4), so PML-I body interiors are not the main sites of TRiC-mediated folding. Furthermore, closed TRiC clustered more often in cryo-tomograms containing a PML-I body (36.6% of particles) than in distal nucleoplasm (17.1%; Supplementary Table 2; p = 0.07, two-sided Mann-Whitney U test).

## Identification of PA28 single-capped proteasomes by multi-template matching

Cylindrical densities approximately 15 nm in diameter, the size of the barrel-shaped 20S proteasome core, were also present in the cryo-tomograms (Extended Data Fig. 1f). PA28-capped proteasomes have been reported to accumulate at PML bodies after interferon γ or arsenic treatment[15,29], so we searched for them with seven proteasome templates, the uncapped 20S core and single- and double-capped PA28 (PA28αβ on an immunoproteasome core), PA200 and 19S (Supplementary Table 3; Supplementary Note 1; Supplementary Video 4). At positions detected by more than one template the cap was assigned by CC rank. Double-capped templates won no positions and the 19S templates fewer than 16, so neither was pursued (Extended Data Fig. 4; Supplementary Note 1). Single-capped PA28 scored highest of the cap-containing templates, but a cap alone is easily confused with other densities of similar size, so we kept only cap detections that overlapped a 20S core detection within 10 nm (Extended Data Fig. 4; Supplementary Note 1). This two-template filter gave 875 PA28 single-capped proteasomes, and STA with 3D classification produced a map of 389 particles at 29 Å resolution in which both the 20S barrel and the PA28 cap were resolved (Fig. 3n–p; Supplementary Fig. 5c–f) and which matched the densities when mapped back onto the cryo-tomograms (Supplementary Fig. 5d,e). At this resolution PA28αβ cannot be distinguished from the nuclear PA28γ homoheptamer, nor an immunoproteasome core from a constitutive one, so we refer to these particles as PA28-capped proteasomes without assigning subunit composition.

Moreover, mapped onto the five segmented PML-I bodies, PA28 proteasomes lay mostly outside the body (13 of 167, 7.8% inside; Supplementary Figs. 3 and 4), a smaller interior fraction than TRiC (14.4%), and showed little spatial clustering, the two largest clusters containing 52 and 15 particles (Supplementary Fig. 6a–c).

## Molecular architecture of nucleosome core particles within PML-I cryo-tomograms

To determine whether chromatin occupies PML-I body interiors, we searched for nucleosome core particles with a cryo-EM derived template (EMDB-8140; Supplementary Video 5). STA of 5,517 particles with 3D classification gave a nucleosome map at 19 Å resolution (957 particles; Fig. 4a–c; Extended Data Fig. 5d,g; Supplementary Video 10) in which the DNA strands and their major grooves were clearly visible (Fig. 4b,c; Supplementary Video 10), localising chromatin in PML bodies for the first time. A second class of 777 particles carried an extra density beside the nucleosome (Extended Data Fig. 5e,f,

asterisk), consistent with bound accessory proteins[43]. Both classes mapped back onto high-contrast densities in the cryo-tomograms (Fig. 4d–f; Supplementary Video 11).

**Columnar open trinucleosomes are observed within PML-I bodies**

Higher-order chromatin folding, long modelled *in vitro* as two-start zigzag[44] or one-start solenoid[45] fibres, has only recently been examined *in situ*, where native chromatin appears as flexible, variable multinucleosome arrangements rather than ordered fibres[46–48], and direct *in situ* evidence for an ordered columnar trinucleosome[49] has been lacking. We therefore also searched our cryo-tomograms with the open-state columnar trinucleosome structure (PDB 7V9S; see Methods). Peaks with strong cross-correlation matched high-contrast densities of multinucleosome assemblies with unusual relative orientations (Supplementary Videos 6–8).

STA of approximately 2,800 particles gave a map of a columnar trinucleosome at 25 Å resolution (Fig. 4h,i; Extended Data Fig. 6i; Supplementary Video 12) and phase randomisation beyond 43 Å showed the estimate was not inflated by overfitting. The trinucleosome is likely flexible, so we then refined and classified with a mask on the top open nucleosome. This gave a 19 Å map with clearly visible major grooves and DNA strands that were absent from the 40 Å low-pass filtered template (Fig. 4j,k; Extended Data Fig. 6d–g,j), and a subsequent global refinement recovered the whole trinucleosome (Extended Data Fig. 6h). Mapped back onto the cryo-tomograms, the particles coincided with high-contrast densities of unusual trinucleosome assemblies (Fig. 4g; Supplementary Videos 6–8).

To test that the third nucleosome is real rather than imposed by the template, we repeated the template matching with a modified 7V9S in which an artificial hole had been cut into the top nucleosome (Extended Data Fig. 7a). The original and hole templates yielded 2,821 and 1,769 particles respectively. Of these, 1,458 pairs lay within 10 nm, and 1,371 (94.0%) had consistent orientations (mean angular deviation 8.9°), so the detections are reproducible rather than template-specific. STA of these 1,371 particles recovered density at the position of the hole (Extended Data Fig. 7c,d), which cannot have come from the reference. In conclusion, the map shows continuous linker DNA joining adjacent nucleosomes (Fig. 4h), which argues against three independent mononucleosomes in incidental proximity and DNA features emerged at 19 Å that were absent from the 40 Å template (Fig. 4j,k; Extended Data Fig. 6j). Together these results confirm columnar open trinucleosomes *in situ* within intact nuclei, consistent with the *in vitro* cryo-EM architecture[49] and observed here directly for the first time.

## Nucleosomes and trinucleosomes share clustered domains in and around PML-I bodies

Nucleosomes (76/390; 19.5%) and trinucleosomes (143/763; 18.7%) were found inside the five segmented PML-I bodies at comparable rates (Fig. 5a–c,f; Supplementary Figs. 7 and 8). Joint DBSCAN clustering of all 4,045 particles (1,758 nucleosomes in 15 cryo-tomograms; 2,287 trinucleosomes in 13) placed 92.9% in 136 clusters, 111 of which (81.6%) contained both particle types, the fraction expected if the two types were randomly interspersed (83% under label permutation, $p = 0.28$), so mono- and trinucleosomes share the same spatial domains rather than segregating (Extended Data Fig. 8). In the five segmented cryo-tomograms the dominant clusters coincided with the PML body interior or its immediate periphery (Extended Data Fig. 8a–e). Ripley's L function analysis[50] against 200 Monte Carlo simulations of complete spatial randomness placed L(r) above the 95% simulation envelope in all 15 cryo-tomograms with nucleosomes, all 13 with trinucleosomes, and for co-clustering in all 13 where both were present (Supplementary Fig. 9). Moreover, clustering increased with radius over the whole range examined, up to 200 nm.

## Chromatin is retained while large complexes are under-represented

The segmented bodies occupied 16 to 24% of the searched volume in the five cryo-tomograms (see Methods), so by chance alone a similar share of each particle type should lie inside. Nucleosomes and trinucleosomes met this expectation (enrichment 0.93, 95% confidence interval 0.75 to 1.13, and 0.88, 0.76 to 1.01), whereas TRiC was modestly depleted (0.69, 0.49 to 0.96; binomial test, $p = 0.03$) and PA28-capped proteasomes were depleted 2.4-fold (0.42, 0.25 to 0.69; $p = 0.0001$). When the nucleosome versus PA28 comparison was stratified by cryo-tomogram, a nucleosome remained 2.6 times more likely than a PA28 proteasome to lie inside the body (Cochran–Mantel–Haenszel test, $p = 0.002$). Compared with the other particle types, TRiC fell between nucleosomes and PA28, with 28 of 194 inside against 76 of 390 and 13 of 167, and differed significantly from neither (Fisher's exact test, $p = 0.14$ and $p = 0.07$). Enrichment also varied between bodies, most notably for TRiC, which was enriched 1.6-fold in TS_15 but depleted in the other four, and PA28 was likewise at nucleoplasmic density in TS_15 (1.1) but depleted elsewhere (Fig. 5d,e). Separated by conformation, open TRiC was depleted more than closed (enrichment 0.55 versus 0.76), in the direction expected from its larger size. In addition, pooled PA28 depletion held when the boundary was eroded or dilated by up to 20 nm (enrichment 0.33

to 0.77), although in TS_08, where a group of PA28 lies within 25 nm outside the body face, a 20 nm dilation raised the per-body value from 0.21 to 0.88 (Supplementary Figs. 6a and 10c).

In conclusion, cryo-SR-CLEM placed the PML-I shell at the edge of a finely textured region whose boundary is irregular in outline yet abrupt in texture. Inside it, the fibrous network was 1.3 to 1.5-fold denser than the surrounding nucleoplasm and large dense clusters were 1.6 to 4-fold scarcer. Mono- and trinucleosomes occupied shared domains within and around PML bodies (81.6% of 136 clusters mixed), and chromatin threaded the body interior as freely as the nucleoplasm around it. The interior is therefore a porous meshwork that is no barrier to chromatin but a filter for large soluble complexes, holding TRiC and PA28-capped proteasomes at a fraction of their nucleoplasmic density, a pattern consistent with content selection by size-dependent partitioning.

## Discussion

Our integrated cryo-CLEM and cryo-SR-CLEM approaches show that cryo-ET can visualise and characterise nuclear condensate interiors at molecular resolution. Like PML bodies, other nuclear condensates including paraspeckles and nucleoli display shell-core or multiphase organisation that can be delineated by cryogenic super-resolution correlated light and electron microscopy, and the pipeline described here provides a generalisable framework for investigating their architecture *in situ*.

Applied to PML-I bodies, this approach gave a direct view of their molecular interior *in situ*, revealing a fibrous network that retains nucleosomal chromatin at nucleoplasmic density while under representing large complexes such as PA28-capped 20S proteasomes (2.4-fold depleted), with TRiC showing an intermediate and more variable behaviour. This is consistent with two earlier observations, that the PA28γ ring binds PML and resides in PML bodies[28] while the 20S proteasome itself is found there only after interferon γ or arsenic treatment[15,29], and whether such treatment drives capped proteasomes into the interior will be the subject of further work.

This architecture is consistent with predictions of the phase-separation-coupled-to-percolation (PSCP) framework for multivalent biomolecular condensates[51], whose network-like material properties have been documented *in vitro*[52,53], reframing the PML body from a featureless protein condensate into a chromatin-permissive, structurally heterogeneous compartment whose porous core may drive physical separation of contents by size, with post-translational modifications likely contributing further to compositional specificity.

Our network analysis reveals that the interior mesh is consistently denser than the surrounding nucleoplasm (1.3 to 1.5-fold; Fig. 2f), with longer continuous strands as a consequence of that density

(Supplementary Fig. 1e). PML bodies are well established to concentrate hundreds of small client proteins through SUMO-SIM interactions[4,5], and soluble protein regulators freely partition into the body interior. The fibrous network we resolve is the likely physical substrate of these interactions, a polyvalent SUMO-SIM scaffold on which small clients are retained.

Our observation now extends this picture by placing a structural constraint at the other extreme of the size range, where dense clusters above 20 nm are 1.6 to 4-fold less abundant and PA28 proteasomes are depleted. Nucleosomes and trinucleosomes, however, are not, and we attribute this to their being retained as part of the chromatin polymer rather than entering the body by diffusion. Porous meshwork architectures have recently been resolved by cryo-ET in the pericentriolar material of *C. elegans* centrosomes[37] and in the polar organiser PopZ condensate in bacteria[54,55], and selective permeability has been proposed but not yet observed for stress granules[56]. Together, these examples, alongside our determination of a network structure in PML bodies, suggest that a percolated, porous meshwork may be a general architectural feature of biomolecular condensates. Notably, PML (TRIM19) and TRIM5α are closely related TRIM family members, and TRIM5α similarly forms organised cytoplasmic bodies directly visualised by cryo-ET[34], raising the possibility that such internal network organisation is a conserved property of TRIM family condensates.

Partitioning was not uniform across bodies. In one of the five segmented bodies (TS_15) both TRiC and PA28-capped proteasomes were present at nucleoplasmic density (Supplementary Fig. 10a,b), and the interior fibre density itself varied between bodies, from 4.1 to 5.3% of area. PML bodies are dynamic and change composition with cell cycle stage, stress and SUMOylation state, and it is possible that the plasticity of the interior network governs what enters and leaves a body at a given time.

As well as informing the physical organisation of PML bodies, our TRiC data provide mechanistic insight into nuclear protein folding. We resolve both open and closed TRiC conformations in the nucleus, consistent with an ongoing chaperonin duty cycle within the nuclear environment[42]. The modest depletion of TRiC from the body interior, together with conformation-dependent clustering of closed-state TRiC in the adjacent nucleoplasm, suggests that TRiC-mediated protein folding occurs predominantly in the nucleoplasm around, rather than within, PML-I bodies. This spatial segregation suggests that PML bodies and the protein folding machinery occupy distinct but neighbouring nuclear compartments.

Vault complexes are classically regarded as cytoplasmic, and to our knowledge have not previously been visualised at structural resolution within the nucleus. Our cryo-ET detection of these at the

periphery of PML bodies was corroborated by immunofluorescence against the major vault protein and may reflect a role in nucleocytoplasmic trafficking of associated factors, given established roles for vaults in transport to the nucleus[57], drug resistance[58] and innate immune signalling[59]. The membrane vesicles observed within and adjacent to PML bodies are similarly unexpected for a membrane-less compartment, and characterising them in additional cell types and conditions will be an avenue for future work.

A central finding of this study is the detection of nucleosomes and trinucleosome assemblies within PML-I body interiors. Notably, previous electron spectroscopic imaging (ESI) data suggested that canonical PML body cores lack detectable nucleic acids in chemically fixed samples[27]. The absence of signal in that study likely reflects the local organisation of internalised chromatin, which we now observe, may fall below the sensitivity threshold of ESI, potentially also combined with displacement during chemical fixation[60].

Our precise *in situ* structural observations are consistent with a growing body of evidence that suggests that specific PML body subtypes incorporate DNA[18,21–23], and now extends this catalogue to importantly include nucleosomal chromatin and trinucleosomes. Interestingly, the most successful trinucleosome template used here was derived from a structure of human telomeric chromatin[49], that also bears a columnar arrangement of nucleosomes in an open conformation. This is characterised by a short nucleosome repeat length. The assemblies we have detected within PML-I bodies display this open conformation, and an accessory density was also observed. Further work will be required to resolve these assemblies at higher resolution and to determine which accessory proteins (e.g. TRF-1) can be resolved within the detected structures.

The open-state conformation of these assemblies within and near PML bodies suggests that the PML body chromatin is accessible to chromatin-binding factors. The open state in telomeric chromatin has been suggested to expose the H2A-H2B acidic patch for interaction with chromatin remodellers, SIRT6 and DNA damage response proteins, without requiring decompaction of the surrounding heterochromatin[49]. PML bodies have established roles in the DNA damage response and in chromatin remodelling at specific loci, including telomere maintenance in ALT-positive cells[16,21,22], and the open trinucleosome assemblies observed here are consistent with this regulatory context. Furthermore, PML bodies have been reported to associate with pericentromeric satellite DNA during G2 phase[23], raising the possibility that a subset of the columnar trinucleosome assemblies detected here represents pericentromeric rather than telomeric chromatin. Notably, like the telomeric repeat sequence used to determine the columnar open trinucleosome structure[49], pericentromeric satellite

DNA is characterised by highly repetitive sequences, suggesting that this open conformation may be a general structural feature of repetitive chromatin. Finally, our trinucleosome template (PDB 7V9S) was derived from a reconstituted human telomeric chromatin array, so our in situ detections are consistent with this open-state columnar arrangement but do not by themselves establish telomeric identity or exclude similar assemblies at non-telomeric loci. As our HFF cultures were not cell-cycle synchronised, the precise chromatin context of these assemblies remains to be determined.

## References


1. Banani, S. F., Lee, H. O., Hyman, A. A. & Rosen, M. K. Biomolecular condensates: organizers of cellular biochemistry. *Nat Rev Mol Cell Biol* **18**, 285–298 (2017).

2. Shin, Y. & Brangwynne, C. P. Liquid phase condensation in cell physiology and disease. *Science* **357**, eaaf4382 (2017).

3. Alberti, S., Gladfelter, A. & Mittag, T. Considerations and challenges in studying liquid-liquid phase separation and biomolecular condensates. *Cell* **176**, 419–434 (2019).

4. Banani, S. F. et al. Compositional control of phase-separated cellular bodies. *Cell* **166**, 651–663 (2016).

5. Shen, T. H., Lin, H. K., Scaglioni, P. P., Yung, T. M. & Pandolfi, P. P. The mechanisms of PML-nuclear body formation. *Mol Cell* **24**, 331–339 (2006).

6. Lallemand-Breitenbach, V. & de Thé, H. PML nuclear bodies. *Cold Spring Harb Perspect Biol* **2**, a000661 (2010).

7. Dellaire, G. & Bazett-Jones, D. P. PML nuclear bodies: dynamic sensors of DNA damage and cellular stress. *Bioessays* **26**, 963–977 (2004).

8. de Thé, G., Rivière, M. & Bernhard, W. Examen au microscope électronique de la tumeur VX2 du lapin domestique dérivée du papillome de Shope. *Bull Assoc Fr Etud Cancer* **47**, 570–584 (1960).

9. Monneron, A. & Bernhard, W. Fine structural organization of the interphase nucleus in some mammalian cells. *J Ultrastruct Res* **27**, 266–288 (1969).

10. de Thé, H., Chomienne, C., Lanotte, M., Degos, L. & Dejean, A. The t(15;17) translocation of acute promyelocytic leukaemia fuses the retinoic acid receptor alpha gene to a novel transcribed locus. *Nature* **347**, 558–561 (1990).

11. Kakizuka, A. et al. Chromosomal translocation t(15;17) in human acute promyelocytic leukemia fuses RAR alpha with a novel putative transcription factor, PML. *Cell* **66**, 663–674 (1991).

12. Koken, M. H. et al. The t(15;17) translocation alters a nuclear body in a retinoic acid-reversible fashion. *EMBO J* **13**, 1073–1083 (1994).

13. Dyck, J. A. et al. A novel macromolecular structure is a target of the promyelocyte-retinoic acid receptor oncoprotein. *Cell* **76**, 333–343 (1994).

14. de Thé, H., Pandolfi, P. P. & Chen, Z. Acute Promyelocytic Leukemia: A Paradigm for Oncoprotein-Targeted Cure. *Cancer Cell* **32**, 552–560 (2017).

15. Lallemand-Breitenbach, V. et al. Role of promyelocytic leukemia (PML) sumolation in nuclear body formation, 11S proteasome recruitment, and As2O3-induced PML or PML/retinoic acid receptor alpha degradation. *J Exp Med* **193**, 1361–1372 (2001).

16. Corpet, A. et al. PML nuclear bodies and chromatin dynamics: catch me if you can! *Nucleic Acids Res* **48**, 11890–11912 (2020).

17. Hell, S. & Stelzer, E. H. K. Properties of a 4Pi confocal fluorescence microscope. *J Opt Soc Am A* **9**, 2159–2166 (1992).

18. Lang, M. et al. Three-dimensional organization of promyelocytic leukemia nuclear bodies. *J Cell Sci* **123**, 392–400 (2010).

19. Rousset, C. et al. Correlation-based nanometric localization using lattice SIM2 and dSTORM in PML nuclear bodies validated by calibration spheres. *Biochem Biophys Res Commun* **752**, 151450 (2025).

20. Stremlau, M. et al. The cytoplasmic body component TRIM5alpha restricts HIV-1 infection in Old World monkeys. *Nature* **427**, 848–853 (2004).

21. Yeager, T. R. et al. Telomerase-negative immortalized human cells contain a novel type of promyelocytic leukemia (PML) body. *Cancer Res* **59**, 4175–4179 (1999).

22. Min, J., Wright, W. E. & Shay, J. W. Clustered telomeres in phase-separated nuclear condensates engage mitotic DNA synthesis through BLM and RAD52. *Genes Dev* **33**, 814–827 (2019).

23. Luciani, J. J. et al. PML nuclear bodies are highly organised DNA-protein structures with a function in heterochromatin remodelling at the G2 phase. *J Cell Sci* **119**, 2518–2531 (2006).

24. Scherer, M. et al. Dual signaling via interferon and DNA damage response elicits entrapment by giant PML nuclear bodies. *eLife* **11**, e73006 (2022).

25. Cohen, C. et al. Promyelocytic leukemia (PML) nuclear bodies (NBs) induce latent/quiescent HSV-1 genomes chromatinization through a PML NB/Histone H3.3/H3.3 Chaperone Axis. *PLoS Pathog* **14**, e1007313 (2018).

26. Alandijany, T. et al. Distinct temporal roles for the promyelocytic leukaemia (PML) protein in the sequential regulation of intracellular host immunity to HSV-1 infection. *PLoS Pathog* **14**, e1006769 (2018).

27. Boisvert, F. M., Hendzel, M. J. & Bazett-Jones, D. P. Promyelocytic leukemia (PML) nuclear bodies are protein structures that do not accumulate RNA. *J Cell Biol* **148**, 283–292 (2000).

28. Zannini, L., Buscemi, G., Fontanella, E., Lisanti, S. & Delia, D. REGγ/PA28γ proteasome activator interacts with PML and Chk2 and affects PML nuclear bodies number. *Cell Cycle* **8**, 2399–2407 (2009).

29. Fabunmi, R. P., Wigley, W. C., Thomas, P. J. & DeMartino, G. N. Interferon γ regulates accumulation of the proteasome activator PA28 and immunoproteasomes at nuclear PML bodies. *J Cell Sci* **114**, 29–36 (2001).

30. Cuchet-Lourenço, D. et al. SUMO pathway dependent recruitment of cellular repressors to herpes simplex virus type 1 genomes. *PLoS Pathog* **7**, e1002123 (2011).

31. Brown, J. R. et al. SUMO ligase protein inhibitor of activated STAT1 (PIAS1) is a constituent promyelocytic leukemia nuclear body protein that contributes to the intrinsic antiviral immune response to herpes simplex virus 1. *J Virol* **90**, 5939–5952 (2016).

32. Liu, Y. T. et al. Isotropic reconstruction for electron tomography with deep learning. *Nat Commun* **13**, 6482 (2022).

33. Object Research Systems. Dragonfly (ORS, Montreal, Canada); http://www.theobjects.com/dragonfly

34. Carter, S. D., Mamede, J. I., Hope, T. J. & Jensen, G. J. Correlated cryogenic fluorescence microscopy and electron cryo-tomography shows that exogenous TRIM5α can form hexagonal lattices or autophagy aggregates *in vivo*. *Proc Natl Acad Sci USA* **117**, 29702–29711 (2020).

35. Falckenhayn, J. et al. On-lamella super-resolution cryo-CLEM for cryo-ET enabled by vacuum-free ultra-stable cryogenic fluorescence microscopy. Preprint at https://doi.org/10.64898/2026.04.14.717675 (2026).

36. Stalling, D., Westerhoff, M. & Hege, H.-C. Amira: a highly interactive system for visual data analysis. In *The Visualization Handbook* (eds Hansen, C. D. & Johnson, C. R.) 749–767 (Elsevier, 2005).

37. Tollervey, F., Rios, M. U., Zagoriy, E., Woodruff, J. B. & Mahamid, J. Molecular architectures of centrosomes in *C. elegans* embryos visualized by cryo-electron tomography. *Dev Cell* **60**, 885-900.e5 (2025).

38. Hrabe, T. et al. PyTom: a python-based toolbox for localization of macromolecules in cryo-electron tomograms and subtomogram analysis. *J Struct Biol* **178**, 177–188 (2012).

39. Chaillet, M. L. et al. Extensive angular sampling enables the sensitive localization of macromolecules in electron tomograms. *Int J Mol Sci* **24**, 13375 (2023).

40. napari contributors. napari: a multi-dimensional image viewer for Python. Zenodo https://doi.org/10.5281/zenodo.3555620 (2019).

41. Ester, M., Kriegel, H.-P., Sander, J. & Xu, X. A density-based algorithm for discovering clusters in large spatial databases with noise. In *Proceedings of the 2nd International Conference on Knowledge Discovery and Data Mining (KDD-96)* 226–231 (AAAI Press, 1996).

42. Xing, H. et al. In situ analysis reveals the TRiC duty cycle and PDCD5 as an open-state cofactor. *Nature* **637**, 983–990 (2025).

43. Allis, C. D. & Jenuwein, T. The molecular hallmarks of epigenetic control. *Nat Rev Genet* **17**, 487–500 (2016).

44. Song, F. et al. Cryo-EM study of the chromatin fiber reveals a double helix twisted by tetranucleosomal units. *Science* **344**, 376–380 (2014).

45. Finch, J. T. & Klug, A. Solenoidal model for superstructure in chromatin. *Proc Natl Acad Sci USA* **73**, 1897–1901 (1976).

46. Hou, Z., Nightingale, F., Zhu, Y., MacGregor-Chatwin, C. & Zhang, P. Structure of native chromatin fibres revealed by cryo-ET *in situ*. *Nat Commun* **14**, 6324 (2023).

47. Kreysing, J. P. et al. Molecular architecture of heterochromatin at the nuclear periphery of primary human cells. *Nat Commun* **17**, 5844 (2026).

48. Cai, S., Böck, D., Pilhofer, M. & Gan, L. The *in situ* structures of mono-, di-, and trinucleosomes in human heterochromatin. *Mol Biol Cell* **29**, 2450–2457 (2018).

49. Soman, A. et al. Columnar structure of human telomeric chromatin. *Nature* **609**, 1048–1055 (2022).

50. Martinez-Sanchez, A., Baumeister, W. & Lučić, V. Statistical spatial analysis for cryo-electron tomography. *Comput Methods Programs Biomed* **218**, 106693 (2022).

51. Pappu, R. V., Cohen, S. R., Dar, F., Farag, M. & Kar, M. Phase Transitions of Associative Biomacromolecules. *Chem Rev* **123**, 8945–8987 (2023).

52. Jawerth, L. et al. Protein condensates as aging Maxwell fluids. *Science* **370**, 1317–1323 (2020).

53. Patel, A. et al. A liquid-to-solid phase transition of the ALS protein FUS accelerated by disease mutation. *Cell* **162**, 1066–1077 (2015).

54. Toro-Nahuelpan, M., Plitzko, J. M., Schüler, D. & Pfeiffer, D. In vivo Architecture of the Polar Organizing Protein Z (PopZ) Meshwork in the Alphaproteobacteria Magnetospirillum gryphiswaldense and Caulobacter crescentus. *J Mol Biol* **434**, 167423 (2022).

55. Scholl, D. et al. The filamentous ultrastructure of the PopZ condensate is required for its cellular function. *Nat Struct Mol Biol* **33**, 420–432 (2026).

56. Khong, A. et al. The Stress Granule Transcriptome Reveals Principles of mRNA Accumulation in Stress Granules. *Mol Cell* **68**, 808-820.e5 (2017).

57. Chugani, D. C., Rome, L. H. & Kedersha, N. L. Evidence that vault ribonucleoprotein particles localize to the nuclear pore complex. *J Cell Sci* **106**, 23–29 (1993).

58. Mossink, M. H., van Zon, A., Scheper, R. J., Sonneveld, P. & Wiemer, E. A. C. Vaults: a ribonucleoprotein particle involved in drug resistance? *Oncogene* **22**, 7458–7467 (2003).

59. Berger, W., Steiner, E., Grusch, M., Elbling, L. & Micksche, M. Vaults and the major vault protein: novel roles in signal pathway regulation and immunity. *Cell Mol Life Sci* **66**, 43–61 (2009).

60. Li, Y. et al. The effects of chemical fixation on the cellular nanostructure. *Exp Cell Res* **358**, 253–259 (2017).

61. Carter, S. D. et al. Distinguishing signal from autofluorescence in cryogenic correlated light and electron microscopy of mammalian cells. *J Struct Biol* **201**, 15–25 (2018).

62. Kaufmann, R. et al. Super-resolution microscopy using standard fluorescent proteins in intact cells under cryo-conditions. *Nano Lett* **14**, 4171–4175 (2014).

63. Moser, F. et al. Cryo-SOFI enabling low-dose super-resolution correlative light and electron cryo-microscopy. *Proc Natl Acad Sci USA* **116**, 4804–4809 (2019).

64. Zheng, S. Q. et al. MotionCor2: anisotropic correction of beam-induced motion for improved cryo-electron microscopy. *Nat Methods* **14**, 331–332 (2017).

65. Zheng, S. et al. AreTomo: An integrated software package for automated marker-free, motion-corrected cryo-electron tomographic alignment and reconstruction. *J Struct Biol X* **6**, 100068 (2022).

66. Kimanius, D., Dong, L., Sharov, G., Nakane, T. & Scheres, S. H. W. New tools for automated cryo-EM single-particle analysis in RELION-4.0. *Biochem J* **478**, 4169–4185 (2021).

67. Zivanov, J. et al. A Bayesian approach to single-particle electron cryo-tomography in RELION-4.0. *eLife* **11**, e83724 (2022).

68. Pettersen, E. F. et al. UCSF ChimeraX: Structure visualization for researchers, educators, and developers. *Protein Sci* **30**, 70–82 (2021).

69. Pedregosa, F. et al. Scikit-learn: machine learning in Python. *J Mach Learn Res* **12**, 2825–2830 (2011).

## Acknowledgements

We thank the Beatson Advanced Imaging Resource (RRID: SCR_023875) for imaging support. Cryo-CLEM and cryo-ET data collection were performed at the Multi-User CryoEM Facility at CSSB, supported by the University of Hamburg and DFG grant numbers INST 152/772-1, 152/774-1 and 152/776-1 FUGG; and at the Rosalind Franklin Institute; we thank Thomas Glen and Matthew Case for support with cryo-FIB milling and cryo-ET data collection respectively, facilitated through the Electrifying Life Sciences programme (Wellcome Trust 220526/Z/20/Z). We thank Maud Dumoux for helpful discussions.

## Funding

This work was supported by a UK Research and Innovation Future Leaders Fellowship (MR/W010690/1), a Royal Society Research Grant (RGS\R1\231494) and a Medical Research Council programme grant (MR/Z504464/1) to S.D.C. C.B. was supported by Medical Research Council grant MC_UU_00034/2. R.K. was supported by a Volkswagen Foundation Freigeist Fellowship (91671; 91671-2) and by the Deutsche Forschungsgemeinschaft (DFG) grant number 496128632. The Rosalind Franklin Institute is funded by the UK Research and Innovation through the Engineering and Physical Sciences Research Council (UKRI-EPSRC); Next Generation Chemistry at the Rosalind Franklin Institute has been supported by grants EP/V011 359/1, EP/T012 021/1, EP/X527 245/1. S.D.C. held a sabbatical at the Rosalind Franklin Institute supported by the Electrifying Life Sciences programme (Wellcome Trust 220526/Z/20/Z). The CRUK Scotland Institute is supported by core grants A17196 and A31287 (ROR 03pv69j64).

## Author contributions

S.D.C. conceived and supervised the project. V.P., R.K. and S.D.C. collected the cryo-ET data. I.H. and P.T. performed 3D-SIM. R.K., J.F. and V.P. performed cryo-SR-CLEM. C.B. performed immunofluorescence. V.P., I.H., J.F., C.B., P.T., B.G.D., R.K. and S.D.C. contributed to data analysis, manuscript writing and editing.

## Competing interests

The authors declare no competing interests.

## Data availability

Sub-tomogram averaging maps have been deposited in the Electron Microscopy Data Bank (EMDB) under accession codes EMD-57924 (TRiC closed, 22 Å), EMD-58330 (PA28 single-capped, 29 Å), EMD-57913 (nucleosome, 19 Å), EMD-57971 (trinucleosome focused refinement, 19 Å), and EMD-57970 (trinucleosome full map, 25 Å). Raw cryo-tomographic data have been deposited in the Electron Microscopy Public Image Archive (EMPIAR) under accession code [EMPIAR-XXXXX]. The doxycycline-inducible PML-I human foreskin fibroblast cell line is available upon reasonable request from the corresponding author.

**Code availability**

Analysis scripts used in this study are available in four GitHub repositories, PML body internal network analysis (https://github.com/StephenC07/pml-body-network-analysis); a napari-based PyTOM CC-score threshold viewer (https://github.com/StephenC07/pytom-cc-threshold-viewer); mesh-based PML body visual proteomics (https://github.com/StephenC07/pml-body-visual-proteomics); and the TRiC cluster pair-orientation classification (https://github.com/StephenC07/tric-cluster-orientation-analysis).

**Supplementary information**

Supplementary Note 1 (PA28 single-capped proteasome identification by multi-template matching), Supplementary Figs. 1–10, Supplementary Tables 1–3 and legends for Supplementary Videos 1–12 are provided in the Supplementary Information file. Supplementary Videos 1–12 are provided as separate files.

**Figure legends**

**Fig. 1 | Cryo-CLEM pipeline for *in situ* visualisation of eYFP-PML-I bodies.** a, A representative cryo-fluorescence image of human foreskin fibroblasts (HFFs) stably expressing doxycycline-inducible eYFP-PML-I cultured on gold SiO2 film grids. eYFP-PML-I bodies appear as yellow puncta. Scale bar = 40 µm. b, Plasma ion image of vitrified HFFs. The nucleus is shaded in orange. White arrowheads indicate lamella targeting position. Scale bar = 2 µm. c, Post-milling cryo-fluorescence image of the lamellae. Purple arrows indicate autofluorescence of the platinum (Pt) deposition layer, used as landmarks for cryo-CLEM. White arrows indicate other eYFP-PML-I bodies captured within the lamellae. Pink arrow indicates the eYFP-PML-I body shown in f,g. Scale bar = 2 µm. d, Cryo-EM search map of the same lamellae. Purple arrows indicate the platinum layers. Scale bar = 2 µm. e, Overlay of cryo-fluorescence and cryo-EM search map, enabling precise correlation of eYFP-PML-I signal for tilt-series collection.

Scale bar = 2 μm. f, Denoised cryo-tomogram slice of the eYFP-PML-I body collected at 33,000× magnification indicated by the pink arrow in c. Green arrowheads indicate proteasome clusters; blue arrowhead indicates ribonucleoprotein (RNP)-like structures; orange arrowhead indicates inner densities; pink arrowhead indicates a dense chromatin region. Scale bar = 500 nm. g, Cryo-fluorescence of the eYFP-PML-I body from c overlaid onto the cryo-tomogram slice, showing correlation of fluorescence signal with the finely textured region. Scale bar = 500 nm. h, A different eYFP-PML-I body collected at higher magnification (53,000×) with cryo-fluorescence overlaid onto the cryo-tomogram slice. Scale bar = 150 nm. i, Cryo-tomogram slice through the eYFP-PML-I body in h. Orange arrowhead indicates inner densities; yellow arrowhead indicates the PML body; blue arrowhead indicates RNP-like structures. Scale bar = 150 nm. j, Histogram of single-molecule localisation precision from cryo-SR-CLEM data. k, cryo-SR-CLEM localisations overlaid onto a cryo-ET tomogram slice, demonstrating that the eYFP-PML-I shell resides inside the finely textured region that lacks large granular densities. Scale bar = 200 nm. l, Cryo-tomogram slice with annotation. Yellow arrowhead indicates the PML body; black arrowheads indicate membrane vesicles. Scale bar = 200 nm. m,n, 3D-SIM images of HFFs expressing eYFP-PML-I, showing characteristic hollow shell architecture of PML bodies across the nucleus. Scale bars = 10 μm. o–t, Zoomed 3D-SIM views of individual eYFP-PML-I bodies illustrating morphological diversity: o, classical round body; p, large body with multiple core density chambers; q, small round body; r, figure-of-eight morphology; s, round body with internal density; t, small body with no discernible core. Scale bars = 500 nm. u, Scatter plot showing the number of PML nuclear bodies per cell (n = 16 cells). v, Histogram of eYFP-PML-I body diameters measured from 3D-SIM data. Median = 380 nm (red dashed line). w, Histogram of eYFP-PML-I shell thickness measured from 3D-SIM data. Median = 105 nm (red dashed line).

**Fig. 2 |** The PML-I body interior holds fewer large dense clusters and a denser fibrous network than the nucleoplasm. a, Cryo-CLEM guided segmentation of the PML-I body in TS_03 (cream) with closed TRiC (red), open TRiC (light blue) and PA28 single-capped proteasomes (yellow) mapped back at their refined positions. Scale bar, 100 nm. b, Central slice through the same body (left) and the same slice with dense clusters coloured by equivalent diameter (right; yellow 6 to 15 nm, green 15 to 20 nm, magenta 20 to 30 nm, dark blue above 30 nm); white outline, cryo-CLEM body boundary. Scale bar, 150 nm. c, Dense clusters per μm² inside the body and in the nucleoplasm by size class, mean of five bodies (bars) with each body shown as a symbol (circle TS_01, square TS_03, triangle TS_08, diamond TS_15, inverted triangle TS_16); numbers give the body to nucleoplasm ratio of the means. d, Dense coverage (left) and clusters larger than 20 nm (right) in 10 nm shells against signed distance from the

cryo-CLEM boundary (negative inside); grey, individual bodies; blue, five body mean. e, Representative 300 nm crops inside the body and in the nucleoplasm of TS_03 with the fibre skeleton (orange) traced after masking dense clusters of 15 nm and larger; the percentage gives skeleton pixels per area in the crop. Scale bar, 50 nm. f, Fibre skeleton per area inside and outside the body after masking clusters of 15 nm and larger, five bodies (left; number, ratio of means), and the same measure against distance from the boundary (right). All analyses used IsoNet denoised tomograms and every third slice through the body; see Methods.

**Fig. 3 |** Macromolecular complexes in and around eYFP-PML-I bodies resolved by template matching and subtomogram averaging. a, Cryo-fluorescence of the eYFP-PML-I body overlaid onto the cryo-tomogram slice. Scale bar, 150 nm. b, Cryo-tomogram slice showing the vault complex indicated by the black asterisk in q. Scale bar, 25 nm. c, Cryo-tomogram slice showing the vault complex indicated by the pink asterisk in d and q. Scale bar, 25 nm. d, Cryo-tomogram slice of the eYFP-PML-I body showing the PML body (yellow arrowhead) and the vault complex (pink asterisk). Scale bar, 150 nm. e, eYFP-PML-I channel (green). f, MVP immunofluorescence (red). g, Merged image with DAPI showing colocalisation of eYFP-PML-I and MVP signals across ROIs 1–3 (dashed boxes), with zoomed insets. h, STA map of TRiC in the closed conformation. i, Same as h rendered transparent with PDB 7X6Q fitted. j, Same as i rotated 90°. k, STA map of TRiC in the open conformation. l, Same as k rendered transparent with PDB 7X7Y fitted. m, Same as l rotated 90°. n, STA map of PA28 single-capped proteasome rendered transparent with atomic model fitted (PDB 7DR6). o, Same as n rotated 90°. p, Solid surface map of the PA28 single-capped proteasome. q, STA particles mapped back onto TS_01. Closed TRiC (red), open TRiC (light blue) and PA28 single-capped proteasomes (yellow) are mapped onto the segmented PML body (cream). Pink and black asterisks indicate the vault complexes shown in c and b, respectively. Dashed box indicates the linear TRiC cluster shown in t. Scale bar, 150 nm. r, TRiC cluster in a circular arrangement, shown without labels. s, Same cluster as r rotated 90°, with labelled contact geometries: head-to-equator (H-E, type 1) and equator-to-equator (E-E, types 2 and 3; see also Extended Data Fig. 3h). t, TRiC cluster in a linear arrangement (H-E, type 4).

**Fig. 4 | STA of nucleosomes and open trinucleosomes and their spatial distribution within PML-I cryo-tomograms.** a, STA map of the nucleosome core particle at 19 Å resolution. b, Same as a rendered transparent with PDB 2CV5 fitted into the density. c, Same as b rotated 90°; DNA strands are clearly visible. d, Cryo-tomogram slices (top) and corresponding nucleosome particle positions overlaid (bottom, blue) for four representative particles (1–4) indicated in f. Scale bars = 20 nm. e, Cryo-tomogram slice showing the PML-I body environment in TS_15. Dense chromatin region (purple) and

RNP-like structures (blue arrowheads) are annotated. Yellow arrowhead indicates the PML-I body; black boxes indicate positions 1 and 2 shown in d. Scale bar = 150 nm. f, Three-dimensional visual proteomics map showing nucleosome core particle positions mapped inside the segmented PML body mesh (white). Numbered boxes correspond to representative particles shown in d. g, Cryo-tomogram slices (top) and corresponding open trinucleosome particle positions overlaid (bottom, pink) for six representative particles. Scale bar = 20 nm. h, STA map of the open trinucleosome rendered transparent with PDB 7V9S fitted and displayed as a molecular surface. i, Same as h rotated 90°. j, STA map of the top nucleosome following focused refinement and 3D classification, rendered transparent with PDB 7V9S fitted. k, Same map as in j of the top nucleosome showing resolved DNA major grooves (numbered 1–7).

**Fig. 5 |** Spatial distribution of macromolecular complexes relative to eYFP-PML-I bodies. a–c, Cryo-tomogram slices of TS_01 (a), TS_03 (b) and TS_08 (c) with template-matched particles mapped back at their refined positions. Each panel is a 7 nm average slice; particles within a 30 nm slab centred on it are drawn at their own z. Nucleosomes (blue circles), trinucleosomes (magenta squares), closed TRiC (red hexagons), open TRiC (light blue hexagons) and PA28 single-capped proteasomes (yellow triangles), coloured as in Figs 2a and 3q. Filled markers lie inside the segmented PML body, open markers outside. Dashed yellow line, PML body boundary from the cryo-CLEM segmentation. Scale bars, 100 nm. d, Percentage of each particle type inside the PML body, pooled across the five segmented cryo-tomograms (coloured bars, 95% Wilson confidence intervals), compared with the percentage expected if particles were distributed at random, given the fraction of the sampled volume occupied by the body (grey bars). e, Enrichment inside the body (observed divided by expected) for each cryo-tomogram (markers, as indicated) with the pooled value (black bar). Dashed line, enrichment of 1. f, Trinucleosome (magenta) and nucleosome (blue) STA maps mapped back onto the segmented PML body of TS_03 (white).

## Extended Data figure legends

**Extended Data Fig. 1 | Cryo-CLEM overview and representative high-contrast densities in eYFP-PML-I body cryo-tomograms.** a, Cryo-fluorescence image of a vitrified lamella showing two eYFP-PML-I bodies (TS_01, TS_03) and two positions in the surrounding nucleoplasm without fluorescence (TS_32, TS_132) at which tilt series were collected (dashed boxes). Scale bar = 1 µm. b, TEM overview of the same lamella without the fluorescence overlay; the two PML body positions are boxed (TS_01, TS_03) and cytoplasm and nuclear envelope are labelled. c–h, Representative cryo-tomogram slices

illustrating the morphological diversity of high-contrast densities observed within and adjacent to PML body interiors: capsules (c), granules (d), filaments (e), cylindrical structures (f), large barrels (g), and rings (h). Scale bars = 20 nm.

**Extended Data Fig. 2 | Template matching and STA workflow of open and closed TRiC.** a, CC score distributions open (green, EMDB-18921, n = 580) and closed (pink, EMDB-18913, n = 378) TRiC templates. b, Flowchart illustrating the TRiC conformational state assignment pipeline. Template matching yielded 580 open and 378 closed particle candidates. Overlap detection with a 10 nm tolerance identified 538 unique positions. The remaining 210 overlapping positions were resolved by CC score competition, in which closed TRiC won 167 competitions (79.5%), yielding final sets of 335 closed and 413 open TRiC particles. c, STA workflow for closed TRiC (EMDB-18913), starting from 335 particles. C1 refinement followed by two rounds of 3D classification with 5 and 3 classes respectively. D8 refinement of 297 filtered particles yielded the final reconstruction. d, FSC curve for the closed TRiC STA. Resolution = 22 Å at FSC = 0.143. e, STA workflow for open TRiC (EMDB-18921), starting from 413 particles. Iterative 3D classification, followed by refinement in C1 of 276 filtered particles. f, FSC curve for the open TRiC STA. Resolution = 32 Å at FSC = 0.143.

**Extended Data Fig. 3 | TRiC chaperonin cluster organisation and spatial analysis.** a, Cryo-tomogram slice showing closed TRiC cluster densities. b, Closed TRiC STAs mapped back onto the tomogram (red). c, Cryo-tomogram slice showing an open TRiC cluster density. d, Open TRiC STA mapped back onto the cryo-tomogram (blue). Scale bars = 20 nm. e, Two-dimensional DBSCAN cluster map showing spatial positions of closed TRiC particles, with cluster sizes indicated. f, Distribution of TRiC cluster sizes determined by DBSCAN (eps ≈ 37 nm) for closed (red) and open (blue) TRiC. g, Centre-to-centre distances of mutual nearest-neighbour pairs within 20 nm for closed (red; n=32, mean 17.3 nm) and open (blue; n=2, mean 16.7 nm) TRiC. Black bars indicate the mean. Dashed line indicates TRiC diameter (~17 nm). h, Distance versus orientation scatter plot showing barrel axis angle against pair distance for TRiC contact geometries: closed equator-to-equator (blue circles), closed head-to-equator (yellow circles), closed intermediate (purple diamonds), and open head-to-equator (yellow squares). Dashed lines indicate the TRiC diameter and the 40° barrel-axis threshold. Numbered points (1–4) mark example pairs displayed in Fig. 3s,t.

**Extended Data Fig. 4 | Multi-template matching and validation pipeline for proteasome species.** a, Cross-correlation score distributions for seven proteasome-related templates across 16 cryo-tomograms (n = 7,795 initial detections). Templates are shown on the y-axis: 20S Core (1,468), PA200

(2,335), PA28 (1,659), PA200-Double (362), PA28-Double (213), 19S-Single (402), and 19S-Double (1,356). b, Y-axis angle difference between all inter-template overlapping detections within 10 nm (n = 8,605 pairs across all seven proteasome templates). The bimodal distribution shows two dominant populations: aligned (<40°, 52.4%) and flipped (>140°, 46.5%), consistent with equal-probability detection of the C2-symmetric 20S barrel in both orientations. Only 1.1% of pairs fall between 40-140° (pie chart, right). In Phase 2, each overlap group requires a Core anchor; orientation-validated PA28 and PA200 caps then compete by cross-correlation score, yielding 566 PA28 and 522 PA200 winners. c, Schematic of the three-phase validation pipeline. Phase 1: seven proteasome templates matched across 16 tomograms yield 7,795 detections; spatial overlap analysis with CC-ranked cap assignment excludes 20S Core from competition; double-capped templates (0 winners) and 19S templates (<16 winners) are rejected. Phase 2: CC-ranked cap assignment with orientation filter applied to 20S Core, PA28, and PA200; requiring Core spatial overlap within 10 nm and cap-Core Y-axis angle aligned (<40 deg) or flipped (>140 deg) yields 566 PA28 particles (interpretable STA density) and 522 PA200 particles (uninterpretable STA density); orientation filter removed only 1.5% of particles. Phase 3: simplified two-template approach (Core + PA28 only), requiring PA28 to spatially overlap with 20S Core within 10 nm, yielding 875 validated PA28 particles and 580 core-solo particles (uninterpretable STA density).

**Extended Data Fig. 5 | Nucleosome template matching and STA workflow.** a, Histogram of local cross-correlation (LCC) scores for all extracted particles (teal, n=750) and retained particles (pink, n=161) from tomogram TS_01. The per-tomogram threshold (dashed red line, LCC=0.6301) was set at +0.03 above the mean LCC score. Applying this threshold across all cryo-tomograms yielded 5,517 particles from an initial set of 22,680. b, STA workflow showing the EMDB-8140 template (40 Å low-pass filtered, two orientations), RELION 4.0 initial model generation from 5,517 particles in C1 symmetry, and bin2 refinement. c, First round of 3D classification into 15 classes; the orange-boxed class was selected for a second round of 3D classification and the pink-boxed class contained an extra density. d, Second round of 3D classification in C2 symmetry yielding 957 particles, corresponding to the 19 Å nucleosome reconstruction. e, C1 class of 777 particles; asterisk (*) indicates extra density adjacent to the nucleosome. f, FSC curve for the nucleosome-with-extra-density STA map (777 particles), indicating a resolution of 18 Å at the FSC=0.143 criterion; phases randomised beyond 53 Å. g, Fourier shell correlation (FSC) curve for the nucleosome STA, showing a resolution of 19 Å at the 0.143 criterion.

**Extended Data Fig. 6 | Open trinucleosome STA workflow.** a, Two views (90° apart) of the open trinucleosome template derived from PDB-7V9S, low-pass filtered to 40 Å. b, De novo initial model generated in RELION. c, Map following iterative 3D refinement. d, Illustration of the focused refinement mask applied to the top nucleosome (orange). e, Map following focused refinement. f, 3D classification; the selected class is highlighted in orange. g, Enlarged view of the selected class. h, Final map following unrestricted refinement of the entire trinucleosome complex (2,287 particles), recovering the full complex after confirming that the top nucleosome signal exceeded the resolution of the original template. i, Fourier shell correlation (FSC) curve for the initial trinucleosome refinement, showing a resolution of 25 Å at the 0.143 criterion. j, Fourier shell correlation (FSC) curve for the focused refinement of the top nucleosome, showing a resolution of 19 Å at the 0.143 criterion.

**Extended Data Fig. 7 | Trinucleosome template validation workflow.** a, Schematic of the template validation pipeline. Template matching was performed in PyTOM using both the original 7V9S trinucleosome template (2,821 particles) and a modified template with an artificial hole introduced into the top nucleosome (hole template; 1,769 particles). Spatial overlap detection with a 10 nm tolerance identified 1,458 overlapping positions; unique positions not detected by both templates were excluded (original: 1,363, hole: 311). Y-axis orientation validation (<40°) retained 1,371 overlapping particles in the same orientation, with 87 particles excluded. b, PDB-7V9S filtered to 40 Å, used as the original trinucleosome template. c, De novo initial model generated in RELION from the validated particle set. d, Recovered map following STA, demonstrating that the missing density in the top nucleosome is restored, confirming that the trinucleosome detections represent genuine signal rather than template bias.

**Extended Data Fig. 8 | Combined DBSCAN spatial clustering of nucleosome and trinucleosome particles relative to PML nuclear bodies.** a–e, Top-down projections of DBSCAN clustering results for five segmented tomograms (a, TS_01; b, TS_03; c, TS_08; d, TS_15; e, TS_16). Nucleosome particles are shown as circles; trinucleosome particles are shown as squares. Each colour represents a distinct cluster; the largest cluster per tomogram is shown in red. Cluster particle counts are indicated at each cluster centroid. Grey crosses denote unclustered noise particles. The green filled region and outline indicate the maximum-intensity projection of the PML body segmentation onto the XY plane. DBSCAN parameters: eps = 100 bin4 pixels (~99 nm) for TS_01, TS_03 and TS_16; eps = 75 bin4 pixels (~74 nm) for TS_08 and TS_15; min_samples = 3.

**Table 1 | Cryo-ET data collection and subtomogram averaging statistics**

| | TRiC closed (EMD-57924) | TRiC open (not deposited) | PA28–20S (EMD-58330) | Nucleosome (EMD-57913) | Trinucleosome, full (EMD-57970) | Trinucleosome, focused (EMD-57971) |
|---|---|---|---|---|---|---|
| **Data collection and processing** | | | | | | |
| Magnification | 53,000× | 53,000× | 53,000× | 53,000× | 53,000× | 53,000× |
| Voltage (kV) | 300 | 300 | 300 | 300 | 300 | 300 |
| Energy filter slit width (eV) | 10 | 10 | 10 | 10 | 10 | 10 |
| Electron exposure (e–/Å2) | 100–120 | 100–120 | 100–120 | 100–120 | 100–120 | 100–120 |
| Defocus range (μm) | −4 to −7 | −4 to −7 | −4 to −7 | −4 to −7 | −4 to −7 | −4 to −7 |
| Pixel size (Å) | 2.48 | 2.48 | 2.48 | 2.48 | 2.48 | 2.48 |
| Tilt range / increment | ±60° / 2°, dose-symmetric | ±60° / 2°, dose-symmetric | ±60° / 2°, dose-symmetric | ±60° / 2°, dose-symmetric | ±60° / 2°, dose-symmetric | ±60° / 2°, dose-symmetric |
| Template (EMDB/PDB) | EMDB-18913 | EMDB-18921 | EMDB-30824 + EMDB-4877 | EMDB-8140 | PDB 7V9S | PDB 7V9S |
| Symmetry imposed | D8 | C1 | C1 | C2 | C1 | C1 |
| Initial particles (template matching) | 378 | 580 | 875 | 22,680 | 2,821 | 2,821 |
| Particles imported into RELION 4.0 | 335 | 413 | 875 | 5,517 | 2,821 | 2,821 |
| Final particles | 297 | 276 | 389 | 957 | ~2,800 | 2,287 |
| Map resolution (Å), FSC = 0.143 | 22 | 32 | 29 | 19 | 25 | 19 |
| Model fitted (rigid body) | PDB 7X6Q | PDB 7X7Y | PDB 7DR6 | PDB 2CV5 | PDB 7V9S | PDB 7V9S |

Maps were generated by subtomogram averaging in RELION 4.0 and atomic models were fitted as rigid bodies in ChimeraX; no atomic model refinement was performed. The 777-particle nucleosome class with additional density (18 Å) and the open TRiC map have not been deposited.

## Methods

## Cell culture

Human foreskin fibroblasts (HFFs) stably expressing eYFP-PML-I under doxycycline-inducible control were cultured as previously described[30,31]. Cells were initially maintained with 5 µg/ml hygromycin (Invitrogen, 10687-010) and 1 µg/ml puromycin (Sigma-Aldrich, P8833) for hTERT expression and selection, respectively. During experiments, HFFs were cultured in Minimum Essential Medium Eagle (MEM; Sigma-Aldrich M5650) supplemented with 10% fetal bovine serum, 2 mM L-glutamine (Life Technologies, 25030-024), 1 mM sodium pyruvate (Life Technologies, 11360-039), and 100 U/ml penicillin/streptomycin.

## 3D-SIM

Slides were coated with human fibronectin (20 mg/L) prepared in PBS (-Ca, -Mg). PML cells were grown in 8-well chamber slides and incubated with doxycycline for 7 hours. Cells were then fixed with 4% formaldehyde (diluted in PBS) for 15 minutes and washed twice in PBS, which was then left on. Samples in chamber slides were imaged using a ZEISS Elyra 7 microscope using Zen Black 3.0 SR FP2 software (version 16.0.21.306) with a 63×/1.4 NA oil immersion objective. Images were captured in lattice SIM mode, with a 27.5 µm grating and 13 phases, onto a PCO Edge 4.2 sCMOS camera. Z-stacks were captured at intervals of 110 nm and a 488 nm laser was used at 5% power. Processing was performed using SIM2 in 3D mode with input SNR medium, 5 iterations and regularisation 0, as per Rousset et al.[19].

## Immunofluorescence

HFF eYFP-PML-I cells were seeded onto coverslips at $1\times10^5$ cells per coverslip and induced with 0.1 µg/ml doxycycline for 7 hours. Cells were washed in CSK buffer (10 mM HEPES, 100 mM NaCl, 300 mM sucrose, 3 mM $MgCl_2$, 5 mM EGTA) and fixed/permeabilised in 1.8% formaldehyde and 0.5% Triton X-100 (Sigma-Aldrich, T-9284) for 10 min at RT. Following two PBS washes, coverslips were blocked for 30 min at RT in 0.45 µm-filtered PBS containing 2% FBS. Primary antibodies were applied individually in separate experiments, either anti-Daxx (Upstate, 07-471; 1/50 dilution) or anti-MVP (Sigma-Aldrich, HPA002321; 1/500 dilution) (50 µl per coverslip, inverted staining). Coverslips were washed three times in PBS (5 min each) and incubated with goat anti-rabbit Alexa 555 secondary antibody (Invitrogen, A-21429; 1/1000 dilution). Following three PBS washes, three water washes, and air drying, coverslips were mounted onto glass slides with Citiflour AF1 (Agar Scientific, R1320). Positive controls (Daxx) and negative controls (secondary antibody only) were included in all experiments. Cell nuclei were

counterstained with DAPI (1/1000 dilution; Sigma-Aldrich, D9542). Coverslips were examined using a Zeiss LSM 880 confocal microscope with a 63× Plan-Apochromat oil immersion objective (numerical aperture 1.4) using 405 nm, 488 nm, and 543 nm laser lines.

**Cryo-ET sample preparation**

For cryo-ET sample preparation, Quantifoil SiO2 film R2/2 200-mesh gold grids were treated with laminin for 30-40 minutes and air-dried on Whatman 40 filter paper. Grids were placed in MatTek glass-bottom dishes containing 2 ml culture media. HFFs were seeded onto grids and cultured for 12-14 hours to achieve optimal confluence for pFIB milling. eYFP-PML-I expression was induced by doxycycline treatment for 7 hours prior to vitrification. Vitrification was performed using a Vitrobot Mark IV (FEI). To ensure optimal structural preservation, excess medium was manually blotted from the grid backside using Whatman 40 filter paper 2 minutes before freezing. Subsequently, 3 µl of 8-9% glycerol in culture media was applied to the cell-bearing side as a cryoprotectant. Grids were immediately plunge-frozen in liquid ethane and stored in liquid nitrogen until pFIB milling.

**Arctis cryo-pFIB milling**

For pFIB milling, frozen grids were clipped into autogrids and loaded into the Rosalind Franklin Institute Arctis cryo-pFIB/scanning electron microscope (SEM; Thermo Fisher Scientific). SEM grid montages were collected using MAPS software to assess cell distribution and ice quality. Grids with optimal cell confluence, ice thickness, and structural integrity were selected for further pFIB milling.

**Cryo-fluorescence-guided pFIB target selection**

Selected grids were rotated 180° on the stage to enable imaging with the integrated fluorescence light microscope (iFLM) so the cells were facing the objective. Each grid square was systematically screened to identify cells exhibiting eYFP-PML-I nuclear bodies. The centre positions of nuclei containing eYFP-PML-I bodies were marked in the fluorescence images and their corresponding x,y coordinates were registered in the SEM montage using MAPS. Both green (eYFP-PML-I) and red channels were acquired with 500 ms exposure times to distinguish specific fluorescence from potential autofluorescence sources[61]. Typically, 20 cells with bright eYFP-PML-I bodies were identified in the central region of each grid to ensure sufficient targets for successful lamella preparation.

**Lamellae preparation**

Following fluorescence screening, the stage was rotated 180° back to its original position, placing cells facing the SEM and pFIB columns. A protective platinum layer was applied in three steps, (i) sputter coating with platinum for 2 minutes, (ii) organometallic platinum deposition using the gas injection system (GIS), and (iii) a second sputter coating cycle. This multi-layer coating strategy provided enhanced sample protection and charge dissipation during milling.

For lamella milling, MAPS software guided the stage to fluorescence-identified regions of interest. Ion beam images typically revealed oval-shaped protrusions at cell centres, which we interpreted as nuclei containing eYFP-PML-I bodies (Fig. 1b). To achieve coincident SEM and FIB imaging planes, the stage Z-height was adjusted while monitoring FIB imaging, using grid features and cell boundaries as fiducial markers. Lamella positions were determined based on cellular topology, using features identifiable in the SEM x-y targeting coordinates that could also be visualised in the FIB view, while avoiding grid bars and thick ice accumulations. Lamella preparation was performed using the Thermo Fisher Arctis cryo-pFIB/SEM. Milling utilized both Argon and Xenon plasma ion beams operating at 30 kV accelerating voltage throughout all stages. A systematic multi-stage milling approach was employed with progressive current reduction to minimise beam-induced damage, typically rough milling at 2 nA to remove bulk material, medium milling at 740 pA, fine milling at 200 pA, and sequential polishing steps at 60 pA and 20 pA. This protocol targeted a final lamella thickness of 150 to 200 nm and produced high-quality vitreous surfaces suitable for cryo-electron tomography. Data were collected across three cryo-ET sessions using Xe plasma FIB at 33,000× magnification (session 1), Xe pFIB at 53,000× (session 2), and Ar pFIB at 53,000× (session 3), yielding 13 vitreous lamellae in total. These data derive from six independent experiments, each comprising a separate cell culture and grid preparation followed by cryo-CLEM and cryo-ET.

**Post milling cryo-fluorescence screening of lamellae**

After cryo-pFIB milling completion, each lamella was imaged in both green (eYFP-PML-I) and red channels to confirm retention of fluorescent signal and verify successful targeting of eYFP-PML-I bodies within the milled region. The platinum layer deposited during pFIB milling exhibited strong autofluorescence under cryo-conditions, which together with the lamella edges served as fiducial landmarks for correlating post-milling cryo-fluorescence images with TEM search maps, enabling precise tilt-series targeting. Approximately 40% of lamellae retained detectable eYFP-PML-I signal after milling.

## Cryo-SR-CLEM

Cryo-SR-CLEM was performed on cryo-lamellae using the VULCROM microscope as described in Falckenhayn et al.[35]. A laser intensity of 200 W/cm² of the 488 nm laser was used for fluorescence excitation and stimulation of photo-blinking. Data were recorded over the course of 2.6 h and binned to 500 ms per frame. Cryo-SMLM reconstructions were done as described in Kaufmann et al.[62]. Single eYFP-PML-I molecules were localised with an average precision of 7.7 nm (Fig. 1j). Transformation of coordinate systems for correlation of cryo-SMLM with cryo-ET was done as described in Moser, Pražák et al.[63]. Localisations were overlaid onto cryo-ET tomogram slices to confirm that the eYFP-PML-I shell resides at the periphery of the finely textured body region (Fig. 1k,l).

## Tilt-series collection

Tomographic data were acquired using a Titan Krios G4 transmission electron microscope (Thermo Fisher Scientific) operated at 300 kV, Selectris energy filter, and Falcon 4i direct electron detector. An energy slit width of 10 eV was applied for all acquisitions. Dose-symmetric tilt series were collected using TOMO5 software (v5.17.0.6390, Thermo Fisher Scientific) with an automated image-shift/beam-shift acquisition strategy to maximize throughput. Data were recorded as movies in electron event representation (EER) format. Tilt series were then recorded of eYFP-PML-I body territories in electron counting mode at a magnification of 33,000× and 53,000×. This corresponds to a pixel size of 3.770 Å and 2.48 Å, respectively, at the specimen level. Only the 53,000× data were used for template matching and subtomogram averaging. Typically, the tilt scheme ranged from +60° to -60° in 2° increments. A -12° or -10° offset was applied to account for the lamella pre-tilt. A cumulative electron dose of 100-120 $e^-/Å^2$ was distributed across the tilt series. Target defocus values ranged from -4 to -7 µm.

## Processing of tilt-series and reconstruction of cryo-tomograms

Motion correction and gain reference application for frame movies were performed using MotionCor2[64]. Tilt-series alignment and weighted back-projection tomographic reconstruction were carried out using AreTomo2[65]. Unbinned alignment parameters were exported in IMOD format (.xf transformation files) using the AreTomo2 -OutImod flag. These alignment parameters were subsequently used to generate pseudo-tomograms in RELION 4.0[66,67] for STA. Output tomograms were binned by 4 for subsequent template matching, resulting in a pixel size of 9.92 Å.

**Denoising of cryo-tomograms**

Denoising was performed using IsoNet[32] and total variation (TV) denoising. IsoNet was applied using deconvolution parameters (DeconvStrength = 1.5, SnrFalloff = 1.5). TV denoising was performed in Dragonfly[33] (Object Research Systems, Montreal, Canada).

**Dense cluster analysis**

IsoNet denoised tomograms (9.92 Å per pixel) were analysed on every third slice over the Z range of the cryo-CLEM guided body label (TS_01 slices 131 to 261, TS_03 82 to 245, TS_08 85 to 249, TS_15 91 to 261, TS_16 65 to 241). A vertical reconstruction artefact along the left edge (X < 100 pixels) was masked in every tomogram, and a 60 pixel strip at the right edge, which carries a reconstruction artefact in which fibres and dense clusters are not detected, was masked in every tomogram. Each slice was z scored and band pass filtered as the difference of Gaussians of sigma 5 and 40 pixels. Pixels darker than the slice background mode by more than one standard deviation of the noise were labelled dense (mode and noise s.d. from a smoothed histogram of the band passed slice, the s.d. from pixels brighter than the mode), closed (two iterations) and hole filled, and contiguous clusters were labelled and assigned an equivalent circular diameter, $2(\text{area}/\pi)^{1/2} \times 0.992$ nm. Clusters of 6 nm and above were binned into 6 to 15, 15 to 20, 20 to 30 and above 30 nm classes and counted per μm² inside and outside the body, each cluster assigned by its centroid label; dense coverage is the fraction of pixels labelled dense. Values were pooled over slices for each body, and ratios are quoted as the ratio of the five body means with the per body range. The same analysis on the raw AreTomo2 reconstructions gave the same pattern (Supplementary Fig. 1g). Diameters describe contiguous dense material and were not mapped to molecular sizes.

**Boundary profiles and label sensitivity**

For each slice the signed distance of every pixel from the cryo-CLEM label boundary was computed with a Euclidean distance transform (negative inside the body), and dense coverage, the density of clusters larger than 20 nm and the fibre skeleton density were averaged in 10 nm shells from 120 nm inside to 150 nm outside the boundary, then over slices and bodies. To test the sensitivity of the inside to outside ratios of dense coverage, large cluster density and fibre skeleton density to the boundary position, the label was eroded and dilated by 20 iterations of a cross-shaped structuring element (14 to 20 nm) and the ratios recomputed as means over slices of the per-slice inside to outside fractions; they changed by 0.04 or less in every body (Supplementary Fig. 1f).

## Fibre network analysis

Before skeletonisation, dense clusters were detected on the z-scored slice smoothed with a Gaussian of sigma 5 pixels, without the sigma 40 background subtraction used for the cluster counts, then thresholded, closed and hole-filled as above. Clusters with an equivalent diameter of 15 nm or more were masked. Their pixels, dilated by 2 pixels, were replaced with the local background (Gaussian smoothed, sigma 10 pixels) plus noise matched to the slice, and the patch was smoothed with a 1 pixel Gaussian. Clusters of 6 to 15 nm were left in place. This retained class includes nucleosome sized densities, which are part of the texture being traced; masking every cluster instead gave a density ratio in the same direction (1.34, per body 1.06 to 1.49). The fibrous texture was then traced in a fixed sequence of steps. Each slice was first denoised by total variation (Chambolle) denoising with a weight of 0.05. Regions above the 75th percentile of a large-scale background map (Gaussian sigma 15 pixels) were excluded from the analysis. Local contrast was then equalised by contrast limited adaptive histogram equalisation (clip limit 0.02, kernel 64 pixels). Thin dark features were extracted with a black top-hat transform (disk radius 6 pixels), and the response was thresholded at the 80th percentile of the unmasked pixels. Objects smaller than 10 pixels were removed, nearby fragments were joined by dilation (disk radius 2 pixels) and holes smaller than 50 pixels were filled. The resulting mask was thinned to a one pixel wide skeleton (Zhang-Suen thinning). Skeleton density is the fraction of skeleton pixels within each compartment, summed over all analysed slices, and is reported as the ratio of the five body means with the per body range. To measure strand length, all dense clusters (6 nm and above) were masked in the same way, the skeleton was split into connected pieces (8 connectivity) and the mean piece length in nm was compared inside and outside the body. All network measures are two dimensional texture statistics on denoised slices; fibre identity is not resolved. Image processing used Python 3.11 with NumPy, SciPy and scikit-image 0.25; analysis scripts are available at https://github.com/StephenC07/pml-body-network-analysis.

## Template matching

Template matching was performed using PyTOM v0.7.1 on 4× binned cryo-tomograms (pixel size 9.92 Å). Templates were generated from atomic models using a two-step process. First, PDB structures were converted to density maps at 25 Å resolution using the molmap command in ChimeraX (molmap #1 25 gridSpacing 9.92) with the binned 4 pixel size. Templates were then generated using PyTOM v0.3.1 pytom_create_template.py with the parameters --input-voxel 9.92 --output-voxel 9.92 --centre --ctf-

correction -z [defocus] -a 0.07 -v 300 --Cs 2.7 --flip-phase --invert -b 80 --low-pass 40. The CTF correction parameters corresponded to our microscope settings (spherical aberration Cs = 2.7 mm, amplitude contrast = 0.07, voltage = 300 kV) with tomogram-specific defocus values of 4, 5, 6, and 7 µm.

Templates derived from EMDB density entries were generated using identical parameters minus the molmap step, except the input pixel size was adjusted to match the respective EMDB map pixel size. Spherical masks were generated using PyTOM v0.3 (pytom_create_mask.py -b 96 -o mask.mrc -r # --radius-minor1 # --radius-minor2 # -s 1 --voxel-size 9.92) and resampled using ChimeraX's volume resample command (vop resample #1 onGrid #0).

Template matching was executed using pytom_match_template.py with the parameters -t [template_path] -v [tomogram_path] -m [mask_path] -d [results_directory] -a [tilt_angles_file] --angular-search 7.00 --voxel-size 9.92 --low-pass 40 -g 0 1 2 --search-z --search-x. The tomogram was low-pass filtered to 40 Å during matching (--low-pass 40), the same cut-off applied to the templates. The angular search step of 7.00° provided sufficient sampling while maintaining computational efficiency. The Z-search range was constrained to the lamella thickness to restrict template matching to the cellular volume and exclude false-positive matches from the lamella surfaces or surrounding ice. The X-search range was constrained to avoid reconstruction artefacts generated by AreTomo2. Specific PDB/EMDB accession numbers used in this study are detailed in Supplementary Table 3. Correlation score maps generated by PyTOM were manually inspected using a custom napari viewer. This plugin enabled interactive adjustment of the cross-correlation threshold while simultaneously displaying the corresponding tomographic data. The viewer was used for inspection and threshold selection only and does not itself extract particles. The plugin also supported generation of movies for documentation, with an automated scale bar for spatial reference (available at https://github.com/StephenC07/pytom-cc-threshold-viewer). Candidate particles above the chosen threshold were extracted from the score maps using PyTOM (pytom_extract_candidates.py) and written as RELION 4.0 STAR files with x,y,z coordinates and Euler angles at the unbinned pixel size of 2.48 Å/pixel. STAR files from individual tomograms were subsequently merged into a single combined STAR file using pytom_merge_stars.py prior to import into RELION 4.0.

**Trinucleosome template matching and STA validation.** To validate trinucleosome particles detected by template matching, we employed a dual-template strategy. Two templates were derived from the

7V9S trinucleosome structure, (i) the original intact structure (Extended Data Fig. 7b), yielding 2,821 initial particle candidates, and (ii) a modified template in which an artificial hole was introduced into one nucleosome subunit, yielding a further 1,769 detections. Template matching was performed independently with each template across all 16 tomograms at a pixel size of 9.92 Å. Detections from both templates were cross-referenced and 1,458 overlapping pairs localised within 10 nm of one another were identified. For each overlapping particle pair, orientation consistency was assessed by comparing Y-axis direction vectors derived from the PyTOM ZYZ Euler angles (see the cross-template overlap analysis below). Of the 1,458 pairs, 1,371 exhibited consistent Y-axis orientations (mean angular deviation 8.9°) and were retained; those exceeding the 40° threshold were excluded. The final validated particle set retained only hole-template coordinates and orientations from orientation-consistent overlaps. STA of the hole-modified particles was performed independently, in which an initial model was generated *de novo* in C1 symmetry using 30 vdam mini-batches, followed by refinement at bin2 (4.96 Å/pixel) in C1. Template matching was additionally performed using alternative telomeric nucleosome array structures, a tetranucleosome (PDB-7V9K), and a tetranucleosome in an open state (PDB-7VA4); none yielded a sub-tomogram average exceeding the resolution obtained with PDB-7V9S.

**PyTOM cross-template overlap and orientation analysis.** Each template in this pipeline was first oriented manually in UCSF ChimeraX with its principal axis aligned to the reference Z axis, the TRiC open and closed templates along the chaperonin barrel axis, the seven 20S proteasome templates (20S core, PA28, PA200, 19S-single, 19S-double, PA28-double, PA200-double) along the proteasome barrel axis, and the original and hole-modified 7V9S trinucleosome templates along the stack axis. This common reference orientation ensured that the identical 7° angular sampling grid used by pytom-match-template explored the same orientation space for every template, so that Euler angles of detections from different templates were directly comparable. Template matched particles exported by pytom-match-template were written as STAR files retaining the PyTOM Euler angles in the _rlnAngleRot, _rlnAngleTilt and _rlnAnglePsi columns. PyTOM's proper-Euler ZYZ convention defines the active reference-to-lab rotation as $R = Rz(\psi)\cdot Ry(\theta)\cdot Rz(\varphi)$, with $\varphi$ = rot, $\theta$ = tilt, $\psi$ = psi, and the lab-frame direction of the reference Y axis given by $R\cdot[0, 1, 0]$. All PyTOM-output analyses described below use this matrix; the RELION-refined barrel-axis analysis of TRiC clusters (described below) uses RELION's own matrix, which differs in composition order and must not be confused with the PyTOM expression above. For each pair of template STAR files, particles in the same tomogram were grouped into spatial clusters within a 10 nm radius (unbinned pixel size 2.48 Å). Within every overlap, orientation consistency between detections was assessed by computing the angle between their lab-frame Y axes.

For pairs compared against a C2-symmetric reference (20S proteasome core), overlaps were classified as aligned (Y-axis angle < 40°) or flipped (> 140°) and the remaining pairs excluded, reflecting the barrel's C2 equivalence under 180° flips. For pairs compared against a non-symmetric reference (the original 7V9S trinucleosome template vs. a hole-modified variant of the same template), only the aligned criterion (< 40°) was applied. For TRiC (open vs closed conformations) and for proteasome cap assignment (Phases 1 and 2; Phase 3 used spatial overlap only), the template at each retained overlap was identified as the detection with the highest cross-correlation score (_rlnLCCmax). For TRiC, template matching yielded 378 closed-state and 580 open-state candidates; CC competition resolved 210 overlapping positions, 167 of which (79.5%) were assigned to the closed state, consistent with its higher mean CC score (0.472 versus 0.398), giving 335 closed and 413 open particles. For the trinucleosome, where both templates represent the same structure, no cross-correlation competition was applied; hole-template detections that passed both the spatial overlap and the Y-axis consistency check were retained as the validated particle set.

**STA using RELION 4.0**[66,67]

**TRiC, closed conformation.** 335 particles were imported into RELION 4.0 and an initial model was generated *de novo* in D8 symmetry using 100 vdam mini-batches. Particles were refined at binning 4 in C1. The 3D reference map was reconstructed directly from 2D tilt series projections using the RELION tomo_reconstruct_particle and pseudo-tomograms were produced at bin 2. The reconstructed particle was used as a reference for bin 2 refinement. 3D classification was performed with 7 classes at T=0.5 to remove noise particles, yielding a single good class of 303 particles in C1 followed by a second round of 3D-classification at T=1 with 3 classes, yielding a final class of 297 particles. A final round of refinement was performed in D8, yielding a resolution of 22 Å at FSC = 0.143.

**TRiC, open conformation.** 413 particles were imported into RELION 4.0 and an initial model was generated *de novo* in C1 symmetry using 50 vdam mini-batches. Particles were refined at binning 4 in C1, and the 3D reference map was reconstructed directly from 2D tilt series projections using the RELION tomo_reconstruct_particle, with pseudo-tomograms produced at bin 2. The reconstructed particle was used as a reference for bin 2 refinement. Iterative 3D classification was performed to remove noise particles, a first round with 3 classes at T=1, a second round with 3 classes at T=1,

followed by 2 classes at T=1 and a final round with 2 classes at T=2, yielding 276 particles. A final round of refinement in C1 at binning 2 yielded a resolution of 32 Å at FSC = 0.143.

PA28 single-capped proteasome identification proceeded in three phases (Extended Data Fig. 4; Supplementary Note 1). In Phase 1, detections from the seven proteasome templates were grouped by spatial overlap within 10 nm and the cap at each position was assigned by CC rank; double-capped and 19S templates were rejected at this stage. In Phase 2, PA28 cap detections were retained only when a 20S core detection lay within 10 nm with a consistent Y-axis orientation (aligned or flipped), giving 566 particles. In Phase 3, the orientation filter was omitted and every PA28 cap detection with a 20S core detection within 10 nm was retained, giving 875 particles; Phase 3 was used for the final map and for all spatial analyses.

**PA28, Phase 2.** 566 particles were imported into RELION 4.0 and an initial model was generated *de novo* in C1 symmetry using 50 vdam mini-batches. Particles were refined at bin2 in C1, and the 3D reference map was reconstructed directly from 2D tilt series projections and pseudo-tomograms generated at bin2. A second round of C1 refinement was performed at bin2. 3D classification (T = 2, 3 classes, no angular sampling) identified one interpretable class containing 538 particles. Two further rounds of refinement at bin2 in C1 yielded a final reconstruction at 33 Å resolution (FSC = 0.143 criterion; Supplementary Fig. 5a,b).

**PA28, Phase 3.** 875 particles were imported into RELION 4.0 and an initial model was generated *de novo* in C1 symmetry using 120 vdam mini-batches. Particles were refined at bin4 in C1. The 3D reference map was then reconstructed directly from 2D tilt series projections and pseudo-tomograms were generated at bin2, followed by two rounds of refinement in C1 prior to 3D classification. 3D classification (T = 2, 3 classes, no angular sampling) selected 494 particles; a second round (T = 2, 2 classes, no angular sampling) yielded 421 particles; and a final round (T = 2, 2 classes, no angular sampling) identified a final class of 389 particles. A final round of refinement yielded a reconstruction at 29 Å resolution (FSC = 0.143 criterion; Fig. 3n–p; Supplementary Fig. 5c–f).

**Nucleosome.** Template matching against all 16 tomograms using EMDB-8140 yielded 22,680 initial particle candidates (mean local cross-correlation, LCC = 0.519). To select high-confidence detections, a per-tomogram CC score threshold of mean LCC + 0.03 was applied (0.6301 for TS_01); particles from tomogram TS_162 were additionally excluded owing to the presence of embedded gold fiducials, retaining 5,517 particles (mean LCC = 0.548; Extended Data Fig. 5a). These 5,517 particles were imported into RELION 4.0 and an initial model was generated *de novo* in C1 symmetry using 50 vdam

mini-batches (Extended Data Fig. 5b). Particles were refined at bin4 in C1. The 3D reference map was then reconstructed directly from 2D tilt-series projections and pseudo-tomograms were generated, followed by refinement at bin2 in C1. 3D classification with 15 classes (T = 2, with angular sampling; angular sampling interval 1.8°, local angular search range 15°) identified two classes of interest, 981 particles corresponding to a nucleosome-like density and 777 particles exhibiting extra density at one linker-nucleosome boundary (Extended Data Fig. 5c). The 981-particle class was taken forward into a second round of 3D classification in C2 symmetry (2 classes, T = 1), yielding a final reconstruction of 957 particles. No further classification was performed on the 777-particle extra-density class. Final refinement yielded a 19 Å reconstruction from the 957-particle class and an 18 Å reconstruction from the 777-particle extra-density class (FSC = 0.143 criterion, Extended Data Fig. 5f,g).

**Trinucleosome.** Template matching against all 16 tomograms using PDB-7V9S yielded 2,821 initial particle candidates; particles from tomograms TS_04 and TS_162 were subsequently excluded as CC score peaks in these cryo-tomograms correlated predominantly with noise. These particles were imported into RELION 4.0 and an initial model was generated *de novo* in C1 symmetry using 30 vdam mini-batches. Particles were refined at bin4 in C1 (Extended Data Fig. 6a–c). The 3D reference map was reconstructed directly from 2D tilt-series projections and pseudo-tomograms were generated, followed by a second round of refinement at unbinned pixel size (2.48 Å/pixel) in C1, yielding a reconstruction of the full trinucleosome at 25 Å resolution (FSC = 0.143 criterion); resolution was taken from the masked FSC corrected for mask effects in RELION post-processing, with phases randomised beyond 43 Å (53 Å for the 777-particle nucleosome map). Focused classification was then performed using a cylindrical mask targeting a single nucleosome subunit, generated in ChimeraX[68] using a cylinder, converted to a binary mask, smoothed with a Gaussian filter (σ = 2), and resampled to match the map grid prior to use. Focused 3D classification (5 classes, T = 1, no angular sampling) identified one class containing 2,287 particles; focused refinement on the top nucleosome subunit at bin2 (4.96 Å/pixel) yielded a map at 19 Å resolution (FSC = 0.143 criterion). Final refinement was performed using a trinucleosome mask generated in RELION 4.0 to align the global structure. A total of 2,287 trinucleosome particles were used for spatial clustering analysis. Particles from cryo-tomogram TS_17 were filtered out through 3D-classification prior to clustering, leaving 13 tomograms.

**Spatial analysis of TRiC clusters**

Spatial clustering of TRiC particles was performed independently for each conformational class (closed and open) using DBSCAN[41] (Density-Based Spatial Clustering of Applications with Noise) as implemented in scikit-learn[69]. Particle coordinates were extracted from per-tomogram RELION STAR files and clustering was performed in 3D coordinate space with parameters eps ≈ 37 nm and min_samples = 2. The eps value of ~37 nm was chosen to capture extended clusters in which particles are connected through chains of neighbours; clusters containing two or more particles were retained and unclustered particles were classified as noise. The difference in clustering frequency between closed (88 of 303) and open (16 of 276) particles was tested with a two-sided Fisher's exact test on the 2 × 2 table of clustered versus unclustered particles, and the risk ratio with its 95% confidence interval was obtained by the log method. To test whether clustering frequency differed with proximity to PML-I bodies, tomograms were classified as PML-body-proximal (n = 7) or distal (n = 9) according to whether an eYFP-PML-I body was captured, and the per-tomogram fraction of clustered closed-TRiC particles was compared between groups with a two-sided Mann-Whitney U test. To measure packing distances within clusters, nearest-neighbour distances were calculated for each particle. Only mutual nearest-neighbour pairs were recorded, where both particles identified each other as their closest neighbour, to avoid double counting. This mutual constraint prevents spurious long-distance pairings in clusters containing more than two particles. Centre-to-centre distances were computed in pixels and converted to nanometres (pixel size = 2.48 Å/pixel). Only pairs within 20 nm were retained for distance and orientation analysis, consistent with the cluster threshold used by Xing et al.[42].

To determine the relative orientation of paired TRiC complexes, Euler angles for closed TRiC were taken from D8-symmetry-refined STA output and for open TRiC from C1 refinement (RELION). The barrel axis of each particle was defined as the third row of the RELION rotation matrix A, computed from Euler angles (rot, tilt, psi) following the RELION convention[66]. The barrel axis was taken as barrel = [sin(tilt)cos(rot), sin(tilt)sin(rot), cos(tilt)].

This corresponds to the reference Z-axis (the barrel axis) transformed into tomogram coordinates, consistent with the ChimeraX Z-axis alignment of the TRiC templates during template preparation described above. The angle between barrel axes of paired particles was computed as the arc-cosine of their dot product. Because TRiC possesses D8 point group symmetry, the equatorial C2 elements within D8 render the barrel axis direction ambiguous (the barrel viewed from either end is equivalent). Barrel axis angles were therefore folded to the 0-90 degree range by taking min(angle, 180 - angle). The

connection angles were likewise folded to the 0-90 degree range before the angular thresholds below were applied.

Pairs were classified into three contact geometries based on two angular measurements, (i) the relative barrel axis angle between paired particles, and (ii) the connection angle, defined as the angle between the inter-particle vector and each particle's barrel axis. Equator-to-equator contacts were defined as pairs with aligned barrel axes (relative barrel axis angle < 40 degrees) and connection angles >= 40 degrees for both particles, indicating the inter-particle vector lies perpendicular to the barrel axes. Head-to-head contacts were defined as pairs with aligned barrel axes and connection angles < 20 degrees for both particles, indicating the inter-particle vector lies along the barrel axes. All remaining pairs were classified as head-to-equator. This group comprised pairs with near-perpendicular barrel axes (relative barrel axis angle >= 40 degrees) together with aligned-barrel pairs whose connection angles met neither the head-to-head nor the equator-to-equator criterion. These residual aligned-barrel pairs were classed as intermediate. Code implementing the DBSCAN-based TRiC pair-orientation classification is available at https://github.com/StephenC07/tric-cluster-orientation-analysis.

**DBSCAN clustering analysis for PA28 single-capped proteasome, nucleosomes and trinucleosomes**

To assess the spatial organisation of nucleosome, trinucleosome and PA28 particles, density-based clustering was performed using DBSCAN[41] as implemented in scikit-learn[69] on template matching coordinates scaled to bin4 pixel space (divided by 4), with min_samples = 3. Nucleosomes and trinucleosomes were clustered jointly across the 15 tomograms containing either particle type, with eps = 100 bin4 pixels (~99 nm) for TS_01, TS_03 and TS_16 and 75 bin4 pixels (~74 nm) for all other tomograms, the smaller value chosen to avoid over-merging spatially distinct clusters in more densely populated datasets; a cluster was counted as mixed when it contained at least one particle of each type. The observed fraction of mixed clusters was compared with a random-labelling null obtained by permuting the particle type labels within each tomogram 2,000 times with the cluster assignments fixed. PA28 single-capped proteasomes were clustered separately across all 16 tomograms with eps = 100 bin4 pixels. Particles not assigned to any cluster were classified as noise. Clusters were visualised as top-down projections with individual clusters colour coded and particle counts annotated at cluster centroids.

To formally assess deviation from complete spatial randomness (CSR), the Ripley's L function was computed for nucleosome and trinucleosome particles across 15 and 13 tomograms respectively. The edge-corrected Ripley's K estimator (Ohser–Stoyan) was computed as $K(r) = V / [n(n-1)] \times \Sigma_i\ C(x_i, r) / \omega(x_i, r)$, where $C(x_i, r)$ is the count of other particles within distance r of particle i and $\omega(x_i, r)$ is the fraction of the sphere of radius r centred at $x_i$ that lies within the analysis volume, estimated by Monte Carlo sampling of 400 uniformly distributed sphere-surface points. The L function was derived as $L(r) = \sqrt[3]{}(3K(r) / 4\pi) - r$, such that $L = 0$ for CSR and $L > 0$ indicates clustering. The analysis volume was defined as the bounding box of all detected particles, padded laterally in X and Y by the maximum analysis radius (200 nm). The Z dimension was left unpadded because the lamella surfaces form a hard physical boundary on the accessible volume. Statistical significance was assessed against a pointwise 95% Monte Carlo confidence envelope derived from 200 simulations of n particles uniformly distributed within the same bounding box. Bivariate Ripley's L was computed analogously, counting one particle type within radius r of each particle of the other type, normalised by both particle counts and volume. Analysis distances ranged from 5 to 200 nm in 32 steps; tomograms with fewer than 10 detected particles of a given type were excluded. Analysis was implemented in Python 3 using numpy and scipy.

**PML body segmentation and mesh generation**

PML bodies were manually segmented in Amira using the brush tool (Thermo Fisher Scientific), guided by cryo-CLEM of eYFP-PML-I. Segmentation was performed on IsoNet denoised tomograms (see Denoising of cryo-tomograms) to more clearly discern the boundary between the PML body and nucleoplasm. Isosurface volumes of PML bodies were generated and exported as TIFF label files. These segmented volumes were then processed in Python. The PML body label was reduced to a binary mask (body voxels set to one and all other voxels to zero), and the marching cubes algorithm (scikit-image implementation, isovalue threshold = 0.5) was applied to this binary volume to extract triangulated mesh surfaces. The volume data were reoriented by transposing axes (ZYX to XYZ) to match the RELION XYZ coordinate order used in the particle STAR files prior to surface extraction.

The resulting meshes were constructed as trimesh objects containing vertices and face connectivity information and used as exported, without repair. For one body (TS_16) the surface was supplied as a pre-exported .obj mesh, already in XYZ order, and loaded directly without the TIFF and marching-cubes steps. Particle coordinates (in unbinned pixels, 2.48 Å/px) were divided by 4 to match the bin-4 mesh coordinate space (9.92 Å/px), and inside/outside classification by ray-casting against the triangulated mesh was performed after scaling mesh vertices and particle coordinates to nanometres (0.992 nm per

bin-4 pixel). All spatial analyses (DBSCAN, Ripley's L, mapping onto the body meshes and enrichment) used the particle sets carried in the per tomogram STAR files after 3D classification, namely 1,758 nucleosomes (the 981-particle nucleosome class and the 777-particle extra-density class, before the C2 reclassification of the former), 2,287 trinucleosomes, 389 PA28 single-capped proteasomes, and 303 closed and 276 open TRiC particles, the closed set being the class retained after the first classification round. This classification was applied to the five tomograms with segmented PML bodies (TS_01, TS_03, TS_08, TS_15, TS_16), so the denominators for the reported inside/outside fractions (167 PA28, 194 TRiC, 390 nucleosome and 763 trinucleosome particles) are the counts within these five segmented volumes. Code implementing this mesh-based visual-proteomics pipeline is available at https://github.com/StephenC07/pml-body-visual-proteomics.

**Volume-normalised enrichment analysis**

To compare the observed interior fraction of each particle type with that expected from the volume occupied by the PML-I body, the segmented body volume was computed from the bin4 label volume (for TS_16, by voxelising the exported mesh at bin4 pitch) and expressed as a fraction of the sampled lamella volume, defined as the full cryo-tomogram footprint in X and Y multiplied by the Z range spanned by all detected particles in that cryo-tomogram (115 to 170 nm across the five cryo-tomograms). The body volume was clipped to the same Z range. Two alternative denominators, the three-dimensional bounding box of all detected particles and the footprint multiplied by the Z extent of the segmentation, gave the same conclusions for nucleosomes, TRiC and PA28; for trinucleosomes the modest depletion reached significance only with the alternative denominators (0.84, $p = 0.02$). Expected interior counts were obtained by multiplying the number of particles in each cryo-tomogram by its body volume fraction and summing across cryo-tomograms. Enrichment was defined as the observed interior fraction divided by the pooled expected fraction, with 95% Wilson confidence intervals on the observed fraction and a two-sided exact binomial test against the expected fraction. Differences between particle types were tested with Fisher's exact test on pooled inside/outside counts and with a Cochran–Mantel–Haenszel test stratified by cryo-tomogram. The analysis script is provided with the mesh-based visual-proteomics code. To test the sensitivity of the enrichment to the boundary position, the body label was eroded or dilated by 5, 10 and 20 nm using its signed distance transform, particles were re-counted by voxel lookup and the expected fraction recomputed from the shifted volume. Nucleosome and trinucleosome enrichment remained between 0.87 and 1.00, TRiC between 0.65 and 0.83 and PA28 between 0.33 and 0.77 across all shifts.

**Composite cryo-tomogram slices with mapped-back particles**

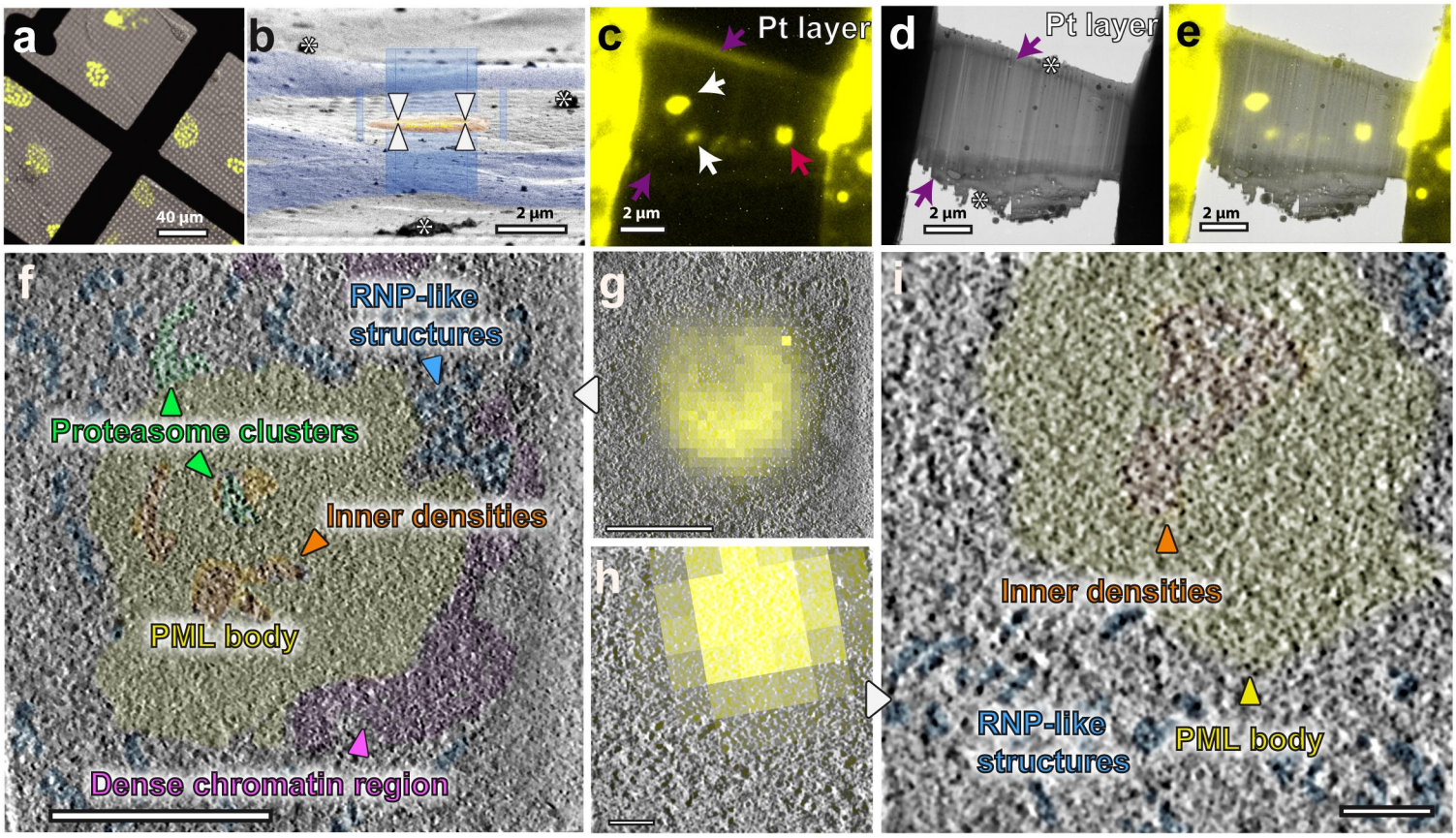
Fig. 5a–c show IsoNet denoised tomograms TS_01, TS_03 and TS_08 at slices 187, 181 and 157, chosen to pass through the body with a large number of particles. Each displayed image is the mean of seven consecutive slices (7 nm) centred on the chosen slice, lightly smoothed (Gaussian, sigma 0.7 pixels), cropped to 800 × 800 pixels (794 nm) around the centroid of the body label and displayed between the 0.5th and 99.5th intensity percentiles. Every template matched particle whose refined centre lay within 15 slices (15 nm) above or below the chosen slice was drawn at its x,y position, and the 29 × 29 pixel neighbourhood around each particle was replaced by the mean of five slices centred on that particle's own z, so that each marker sits on the density it was matched to. Particles were classified as inside or outside the body by looking up the segmentation label at their rounded coordinate, and the boundary drawn is the label contour on the chosen slice.

**Statistics and reproducibility**

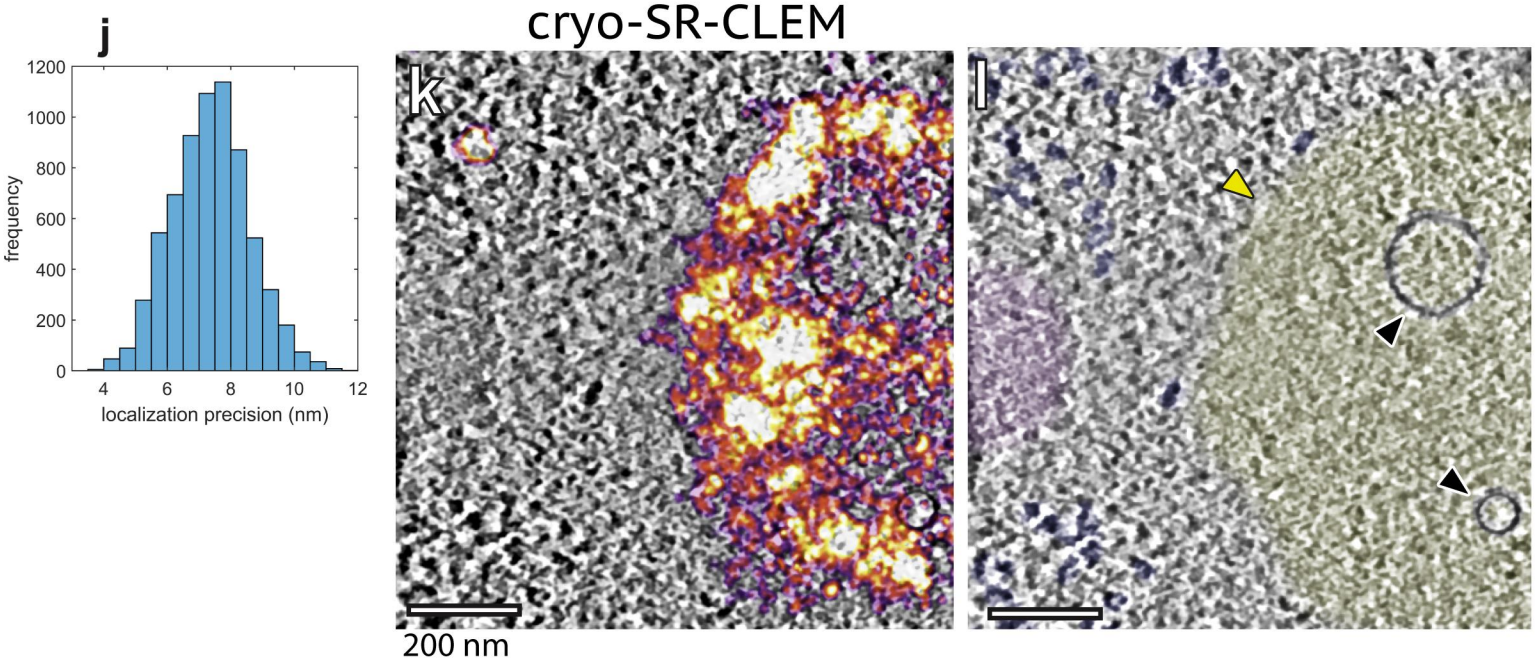
The cryo-ET workflow, from vitrification to tomogram reconstruction, was carried out on six independent batches of cells, imaged in three microscope sessions (Supplementary Table 1). The 16 cryo-tomograms analysed (45 tilt-series from 13 lamellae, five PML-I bodies segmented) come from the two sessions collected at 53,000×, which gave the thinnest lamellae, and their data were pooled for analysis. The 33,000× session contributed to the lamella and tilt-series totals and provided the overview cryo-tomogram in Fig. 1, but none of its data entered template matching or subtomogram averaging. 3D-SIM data were collected from 16 cells in a single preparation, and immunofluorescence was repeated three times with similar results. No statistical method was used to predetermine sample size, which was set by the number of lamellae that retained eYFP-PML-I fluorescence and yielded cryo-tomograms of sufficient quality. The experiments were not randomised and the investigators were not blinded during segmentation, threshold selection or analysis. Two of the seven fluorescence-positive cryo-tomograms (TS_04, TS_162) captured less than 10% of a body and were not segmented. Particle exclusions before subtomogram averaging are described in the relevant sections above. Statistical analyses were performed with SciPy 1.15.3. All tests were two-sided, exact p values are given in the text, and per-body values are reported alongside pooled values since particles within a cryo-tomogram are not independent.

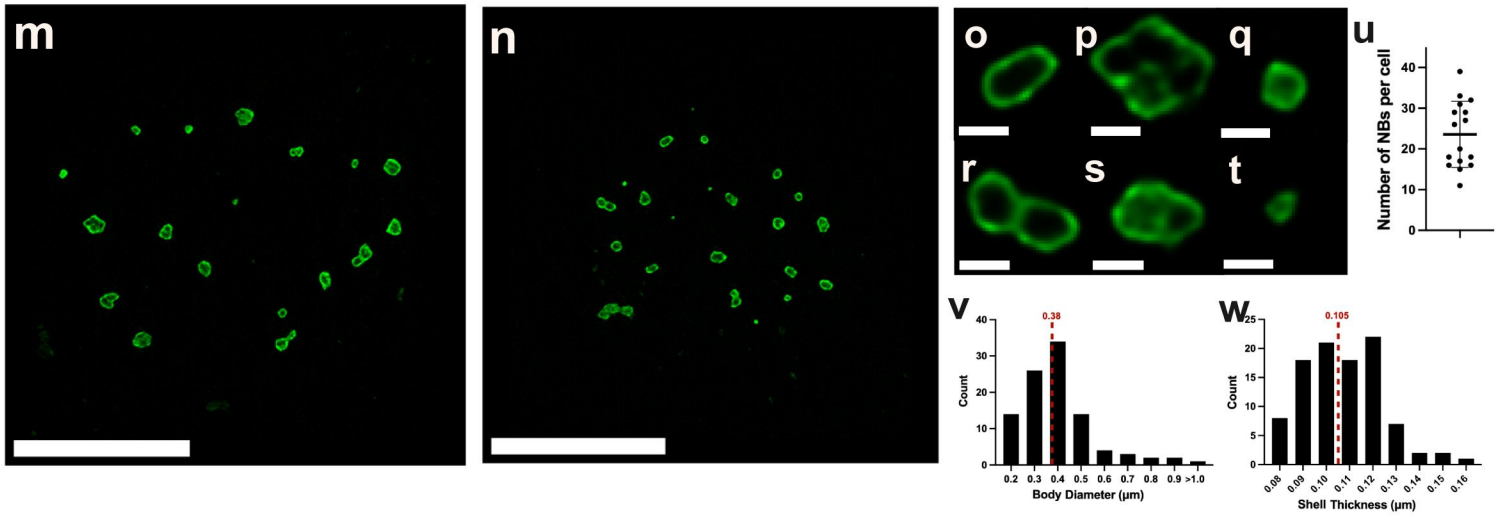
**Use of AI-based tools**

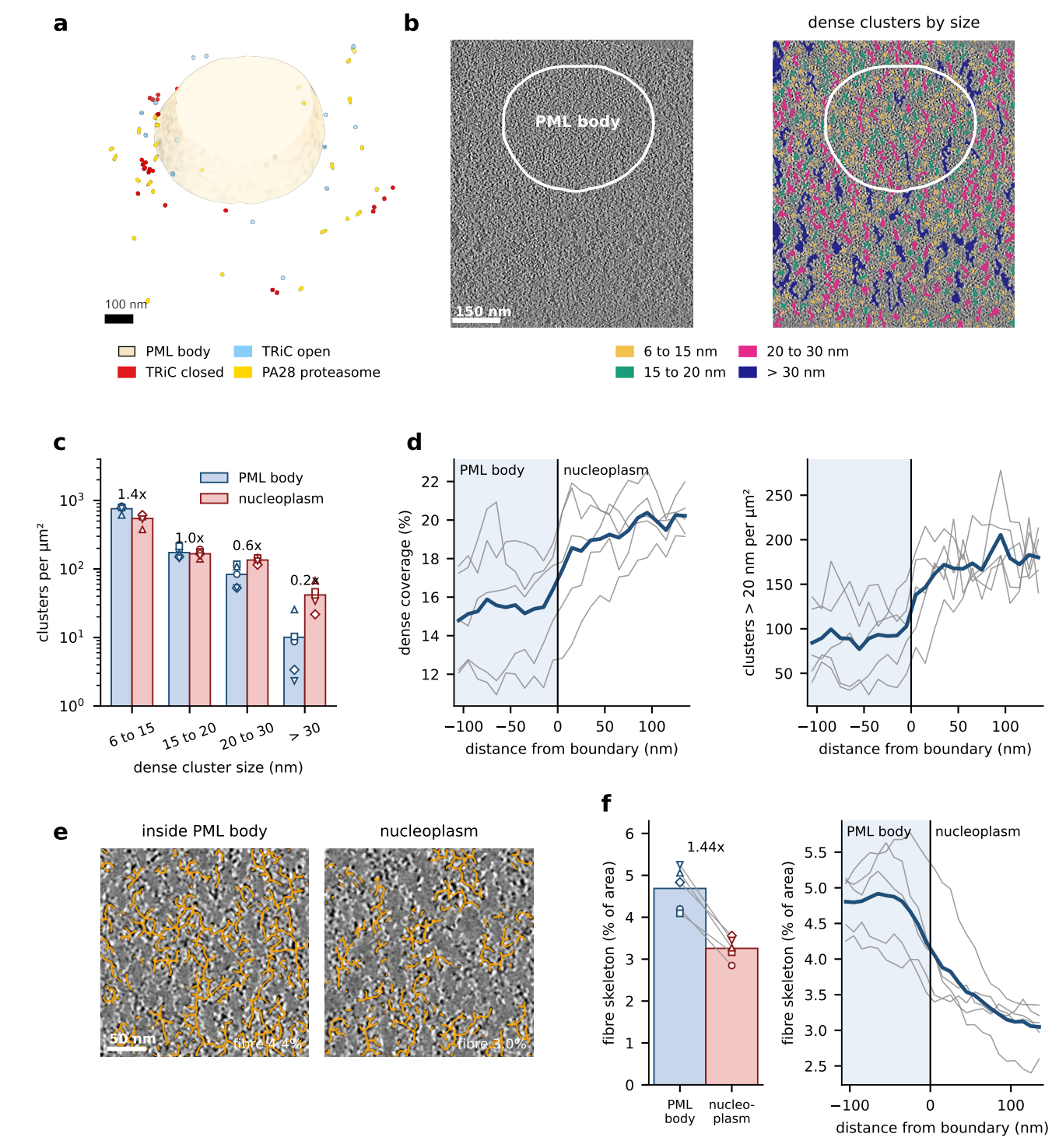
Analysis scripts for the network texture analysis, the volume-normalised enrichment analysis and the assembly of Figs 2 and 5 and Supplementary Figs 1, 3, 4 and 10 were written with the assistance of Claude Code (Anthropic; Claude Opus 4 and Claude Fable 5.1 models). All code was reviewed by the authors, key statistics were recomputed independently, and the scripts are deposited in the repositories listed under Code availability. AI tools were also used for language editing and for cross-checking numbers and references against the text. Conceptual development, interpretation and conclusions are the authors' own.

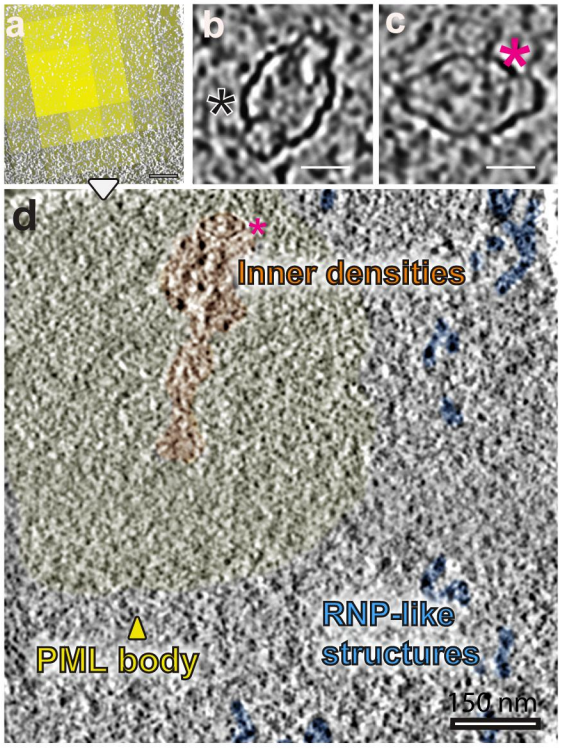

a
40 µm
b
2 µm
c
Pt layer
2 µm
d
Pt layer
2 µm
e
2 µm
f
RNP-like structures
Proteasome clusters
Inner densities
PML body
Dense chromatin region
g
h
i
Inner densities
RNP-like structures
PML body

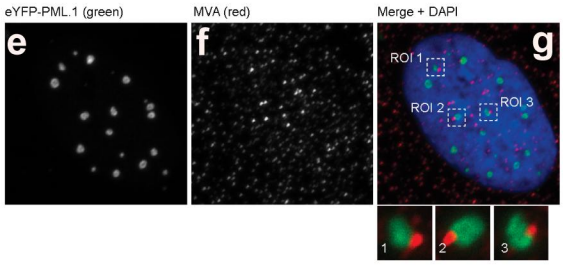
cryo-SR-CLEM

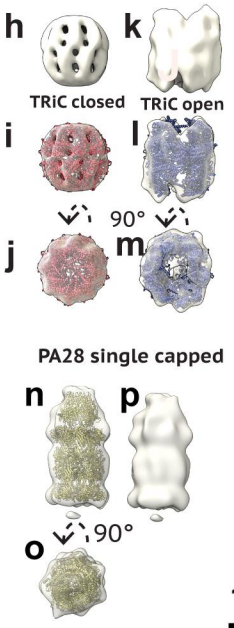

j
frequency
localization precision (nm)
k
l
200 nm

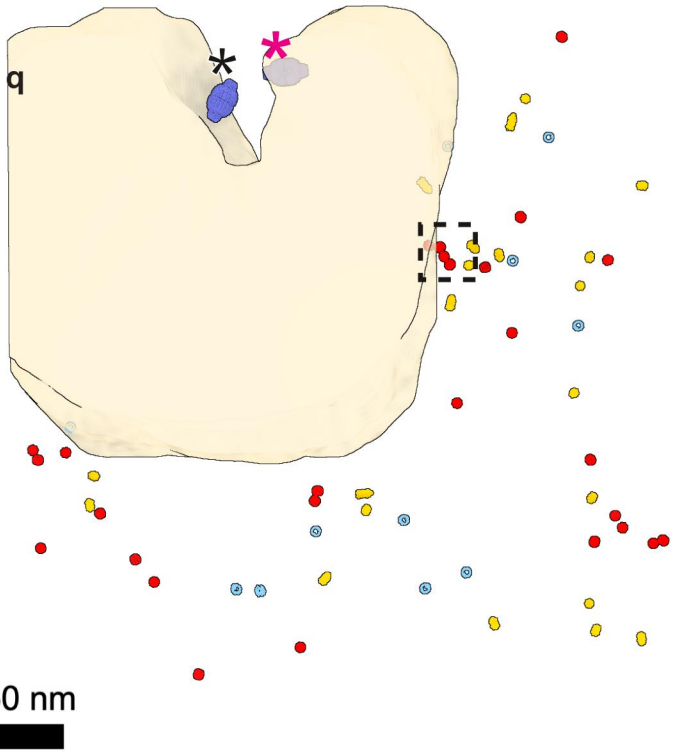

m
n
o
p
q
r
s
t
u
Number of NBs per cell
v
Count
Body Diameter (µm)
w
Count
Shell Thickness (µm)

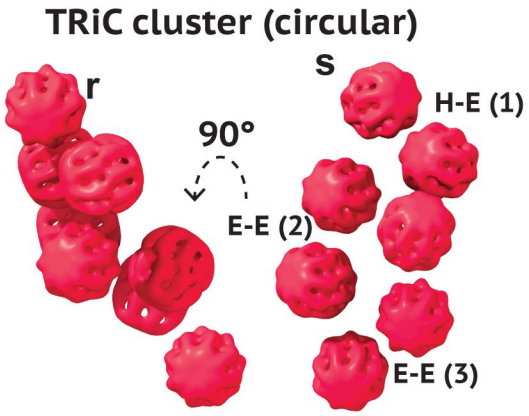

a
100 nm
PML body
TRiC closed
TRiC open
PA28 proteasome
b
PML body
150 nm
dense clusters by size
6 to 15 nm
15 to 20 nm
20 to 30 nm
> 30 nm
c
PML body
nucleoplasm
1.4x
1.0x
0.6x
0.2x
clusters per µm²
6 to 15
15 to 20
20 to 30
> 30
dense cluster size (nm)
d
PML body
nucleoplasm
dense coverage (%)
distance from boundary (nm)
clusters > 20 nm per µm²
distance from boundary (nm)
e
inside PML body
nucleoplasm
50 nm
fibre 4.4%
fibre 3.0%
f
1.44x
fibre skeleton (% of area)
PML body
nucleo-plasm
PML body
nucleoplasm
fibre skeleton (% of area)
distance from boundary (nm)

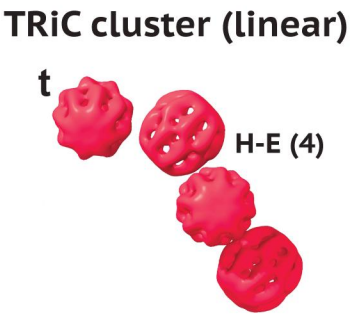

a
b
c
d
Inner densities
PML body
RNP-like
structures
150 nm

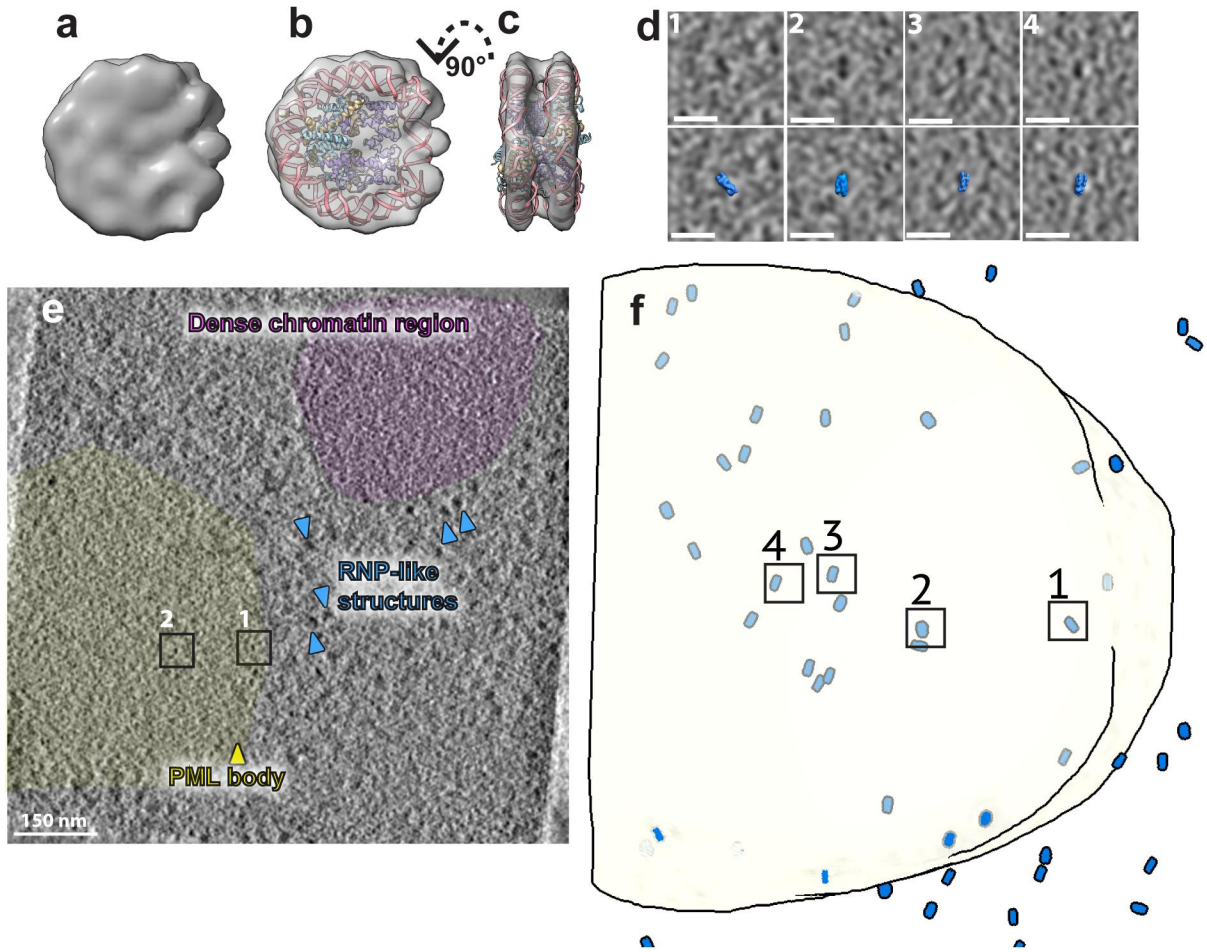

eYFP-PML.1 (green)
MVA (red)
Merge + DAPI
e
f
g
ROI 1
ROI 2
ROI 3
1
2
3

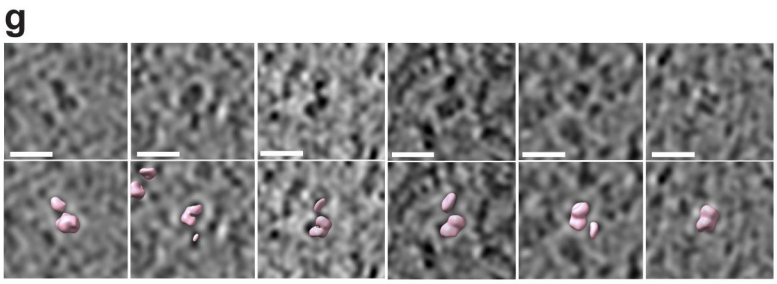

h
k
TRiC closed
TRiC open
i
l
90°
j
m
PA28 single capped
n
p
o
90°

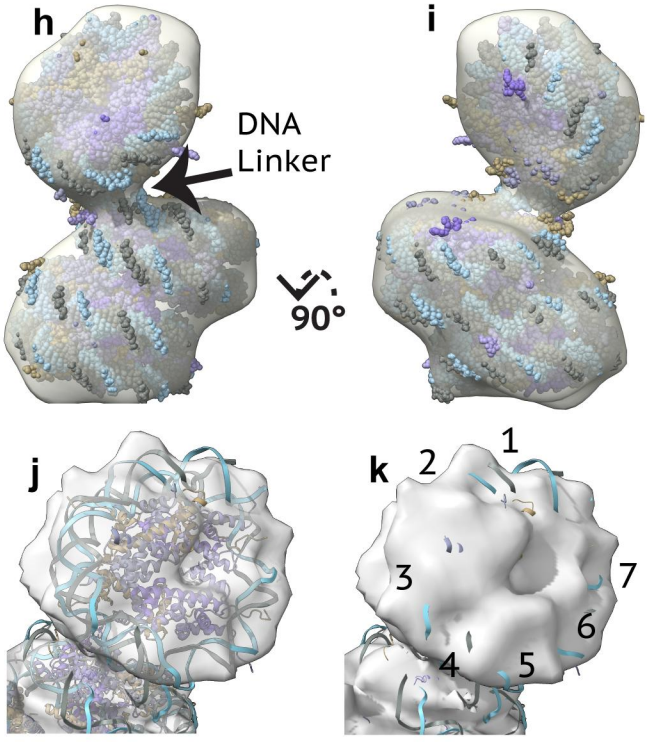

q
150 nm

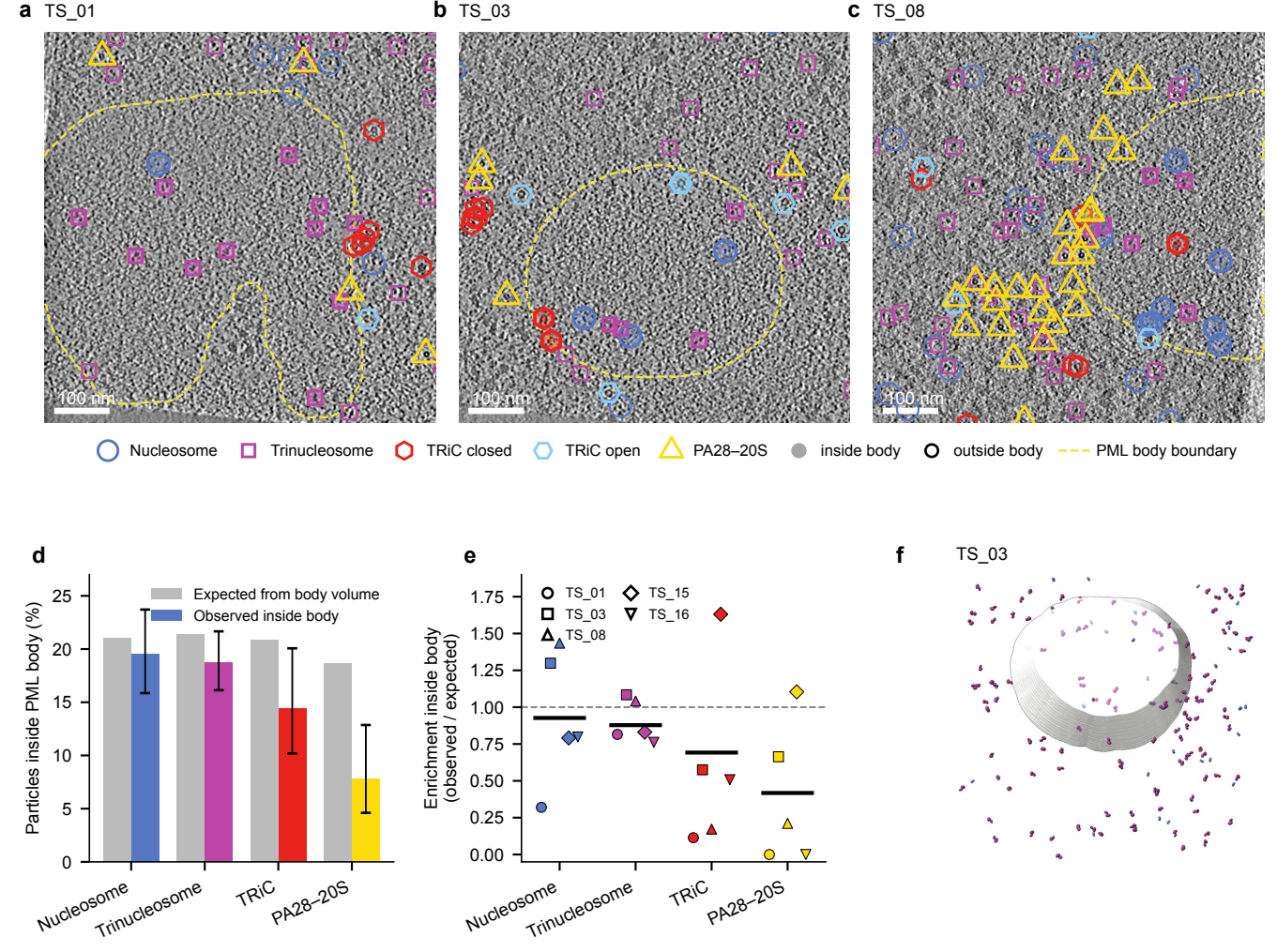

TRiC cluster (circular)
r
s
H-E (1)
90°
E-E (2)
E-E (3)

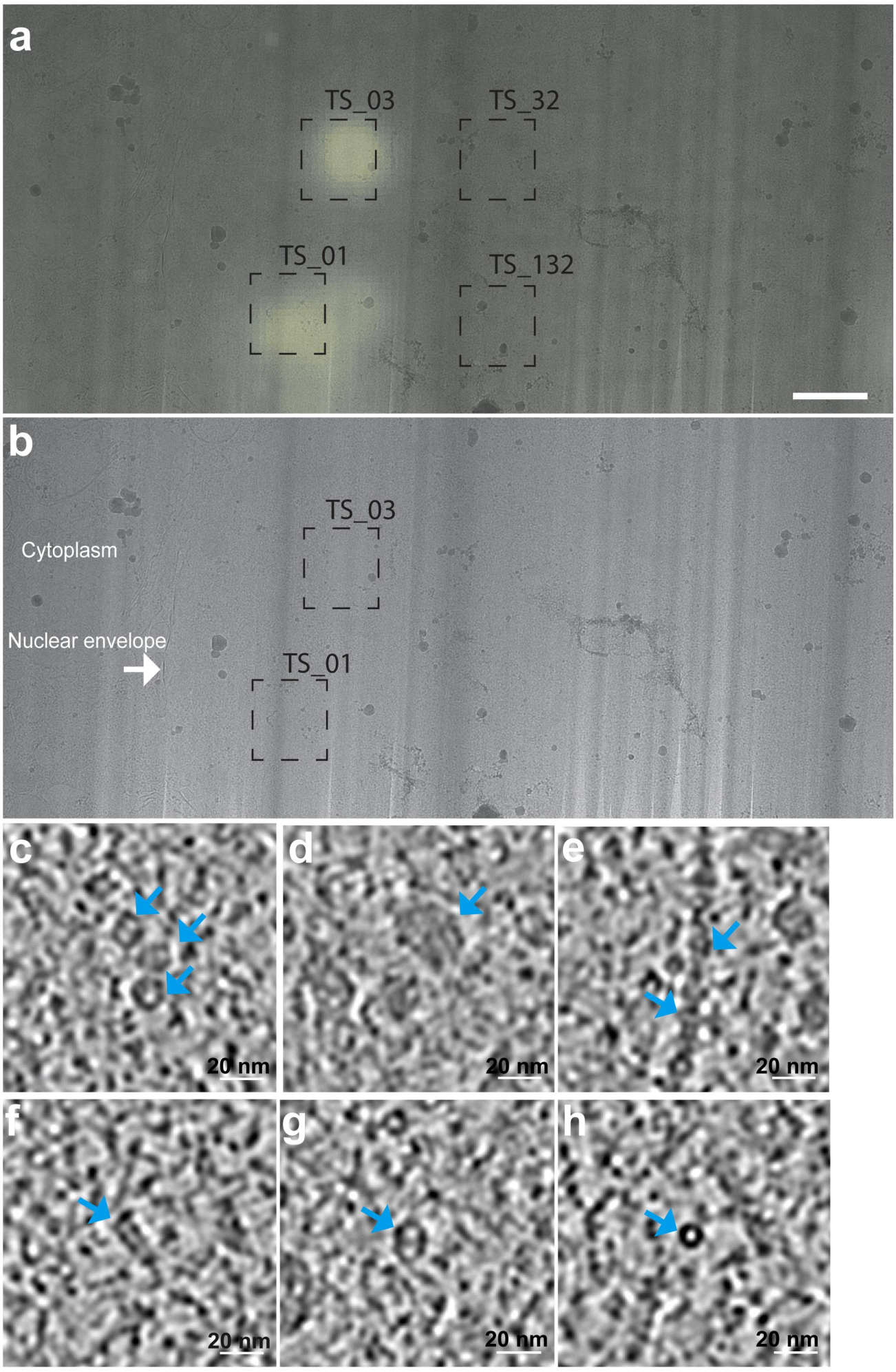

TRiC cluster (linear)
t
H-E (4)


a
b
c
90°
d
1
2
3
4
e
Dense chromatin region
RNP-like structures
2
1
PML body
150 nm
f
4
3
2
1

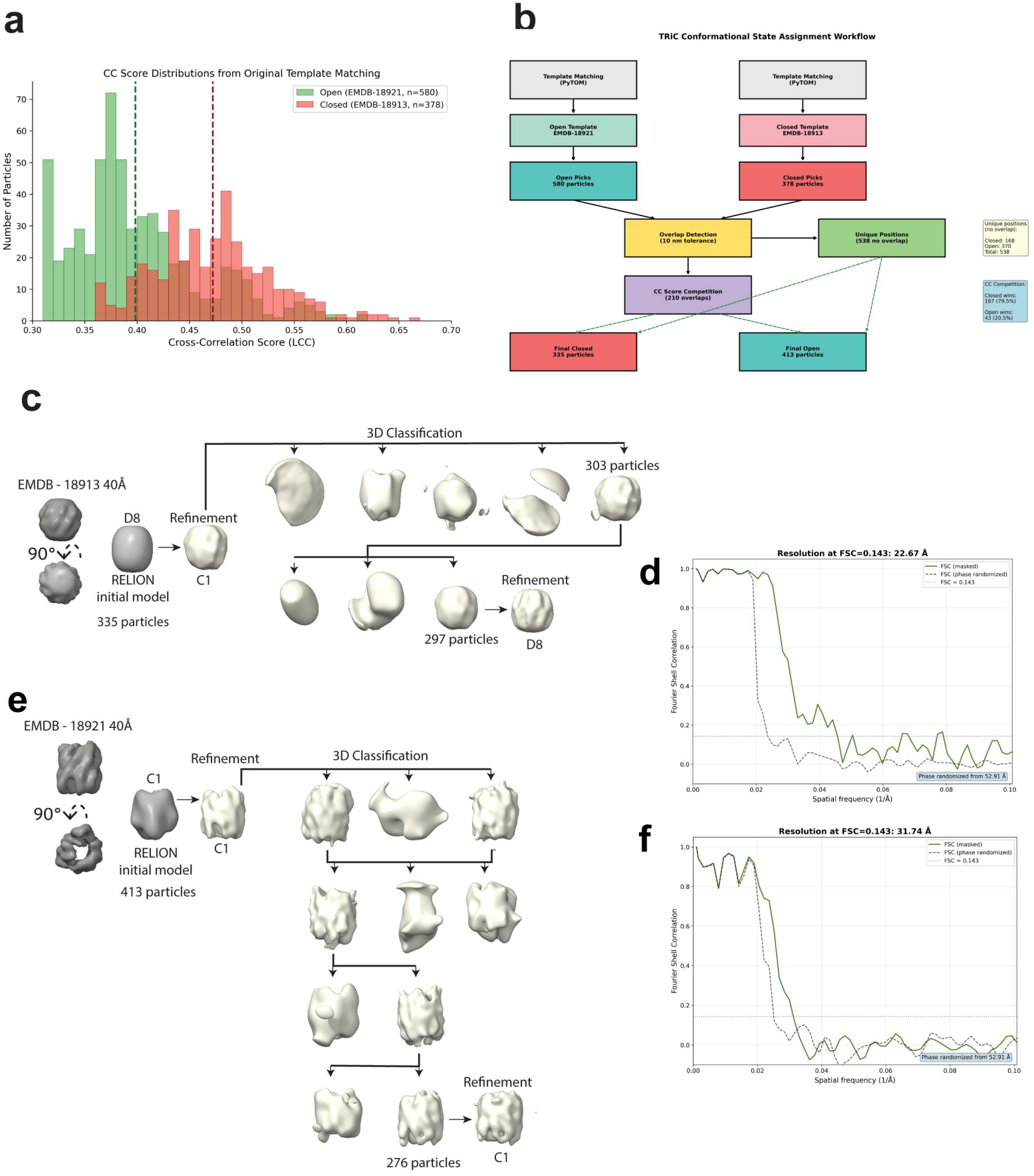

g


h
DNA Linker
90°
i
j
k
1
2
3
4
5
6
7

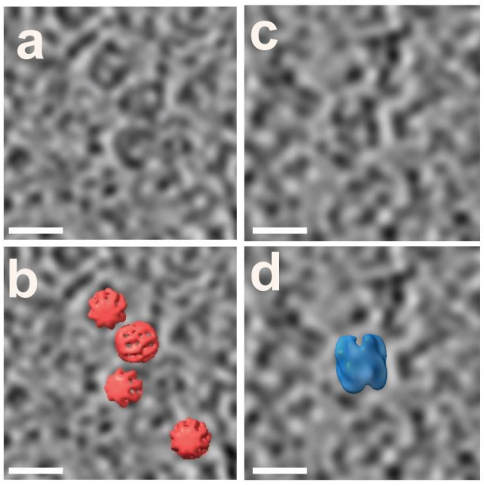

a TS_01
b TS_03
c TS_08
100 nm
Nucleosome
Trinucleosome
TRiC closed
TRiC open
PA28–20S
inside body
outside body
PML body boundary
d
Particles inside PML body (%)
Expected from body volume
Observed inside body
Nucleosome
Trinucleosome
TRiC
PA28–20S
e
Enrichment inside body (observed / expected)
TS_01
TS_03
TS_08
TS_15
TS_16
f
TS_03

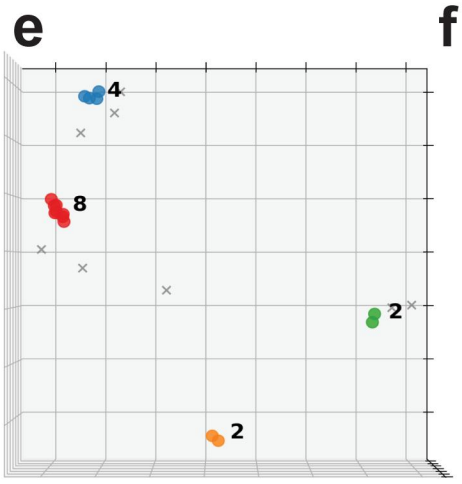


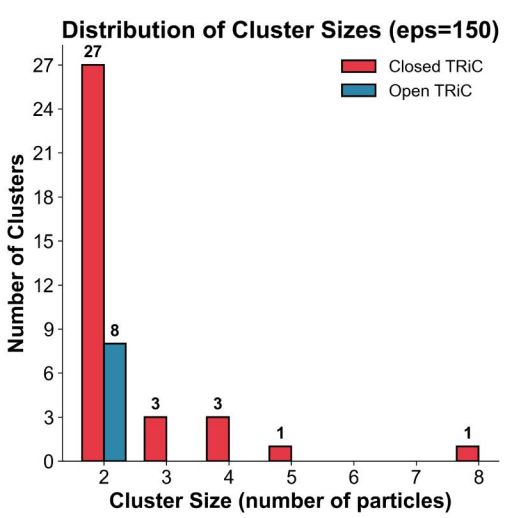

Extended Data Fig. 1

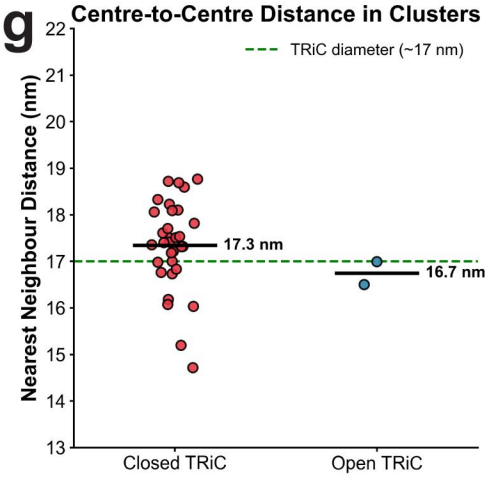


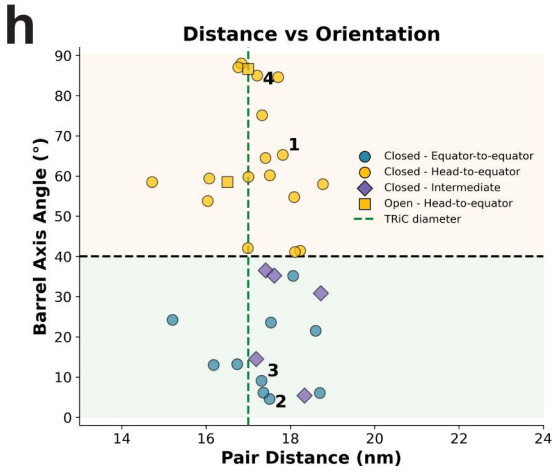

# Extended Data Fig. 2



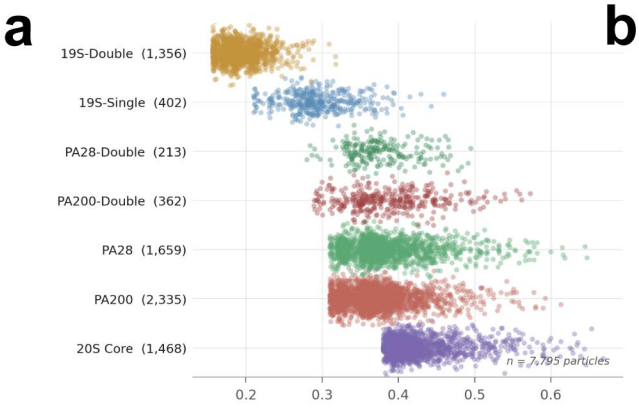



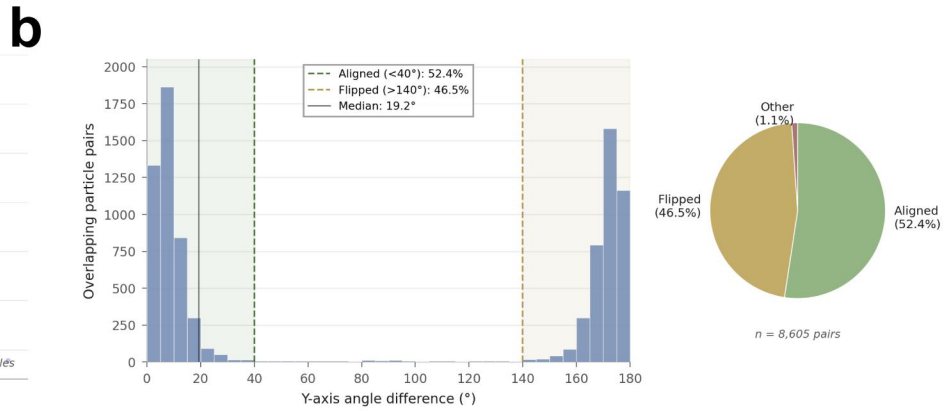




# Extended Data Fig. 3




c

**1 Template matching**

**7 proteasome templates matched across 16 tomograms: 7,795 detections**
**20S Core (1,468) | PA28 (1,659) | PA200 (2,335)**
**19S-single (402) | 19S-double (1,356) | PA28-double (213) | PA200-double (362)**

Spatial overlap analysis using CC-ranked cap assignment:
exclude 20S Core, assign highest-CC cap.

Reject: double caps (0 winners), 19S (<16 winners, 46% solo), overlaps with no 20S Core present.

**2 CC-ranked cap assignment + orientation filter (20S Core, PA28, PA200)**

Require: (i) 20S Core overlap within 10 nm, (ii) cap-Core Y-axis angle
aligned (<40°) or flipped (>140°). Assign cap by highest cross-correlation.

**PA28: 566 particles**
**STA: interpretable density**

*Orientation filter removed only 1.5% of particles.*

**PA200: 522 particles**
**STA: uninterpretable density**

**3 Core + PA28 only (2 templates)**

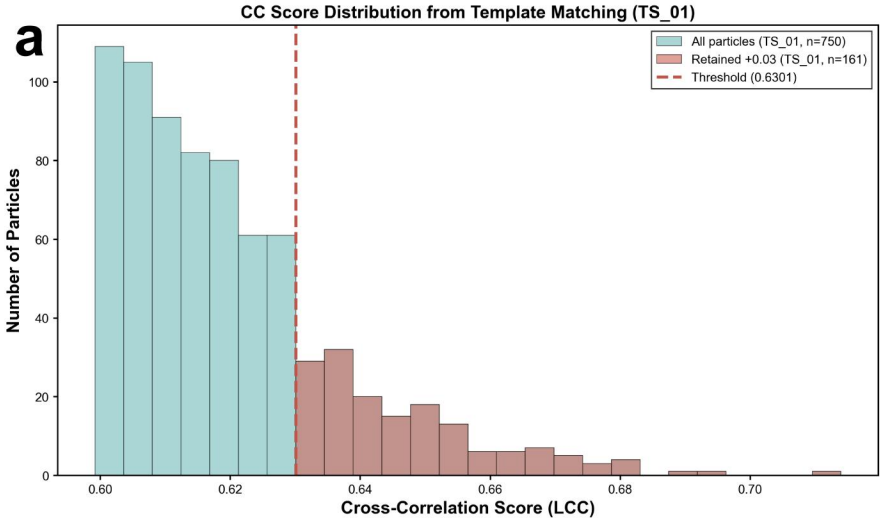
**Rule: PA28 must spatially overlap with 20S Core within 10 nm.**

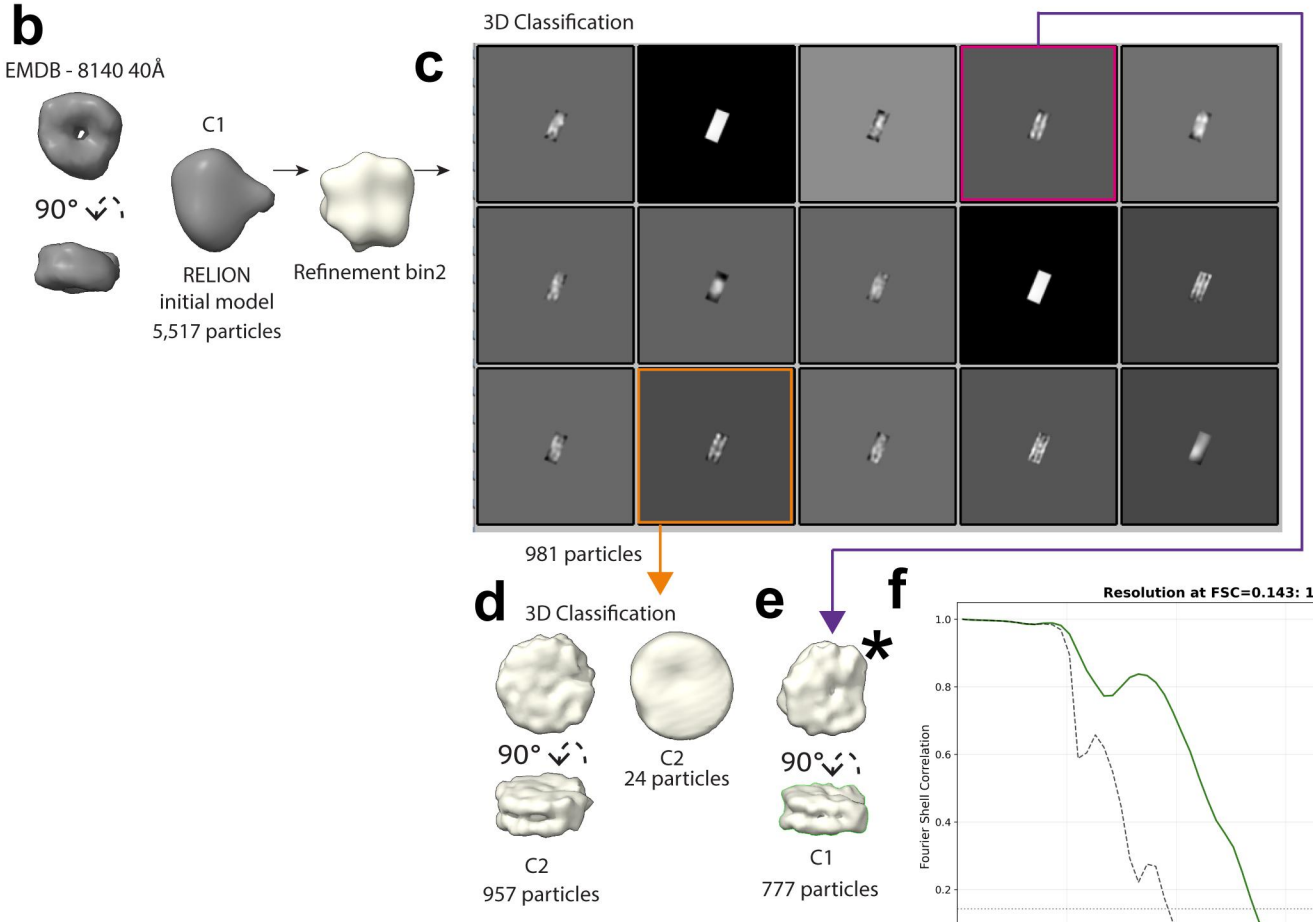
**PA28 validated**
**875 particles**

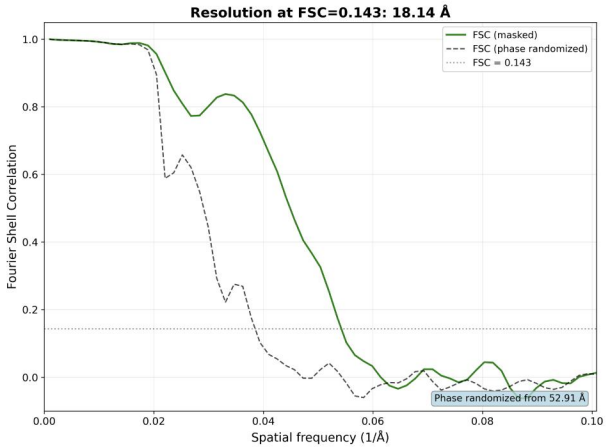
**Core solo: 580 particles**
**STA: uninterpretable density**

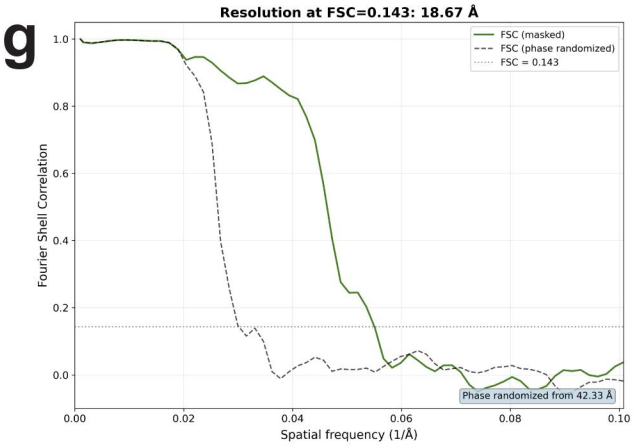
*n = 7,795 initial detections*
*16 tomograms, 2.48 Å/px*

# Extended Data Fig. 4

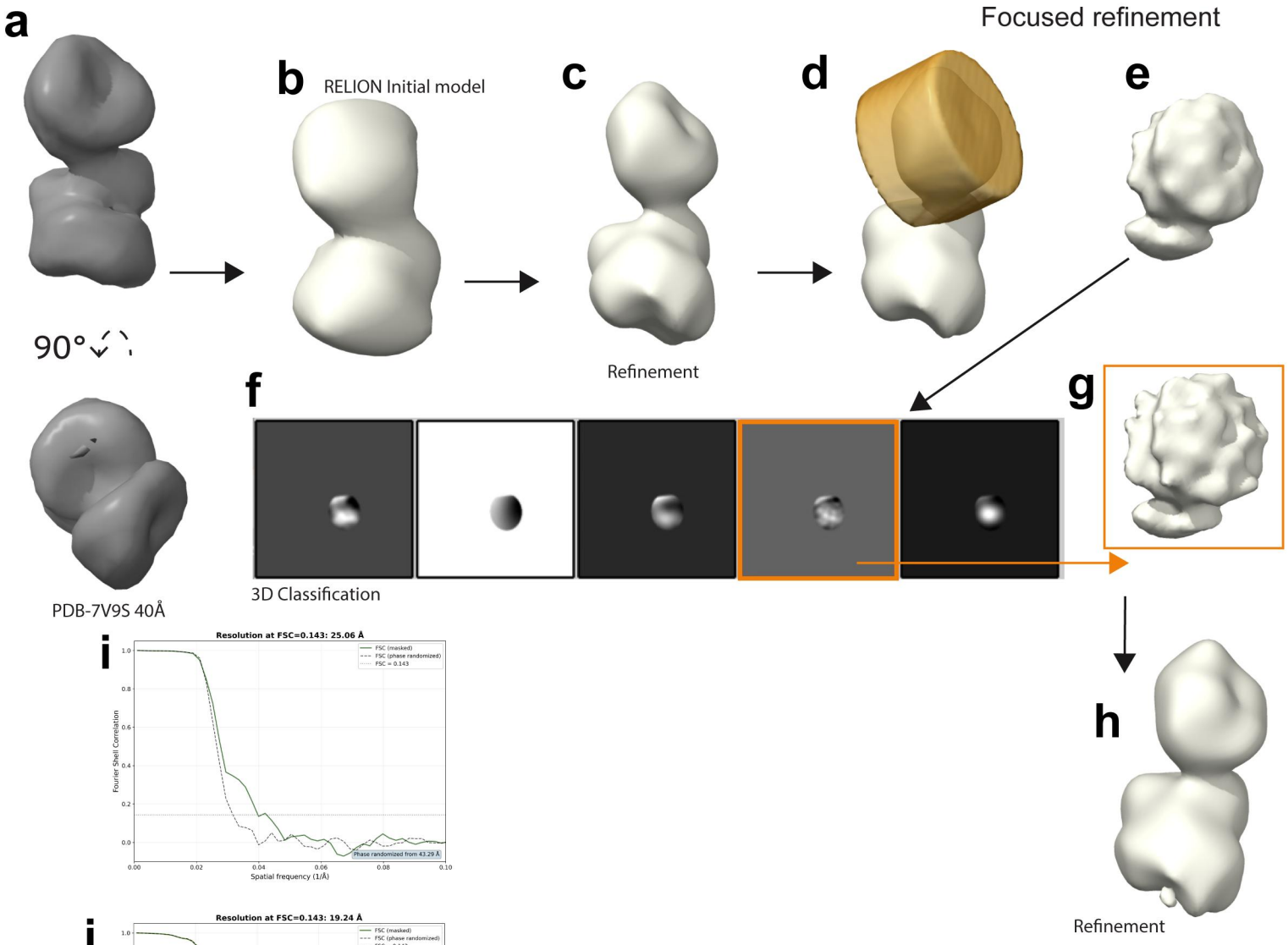


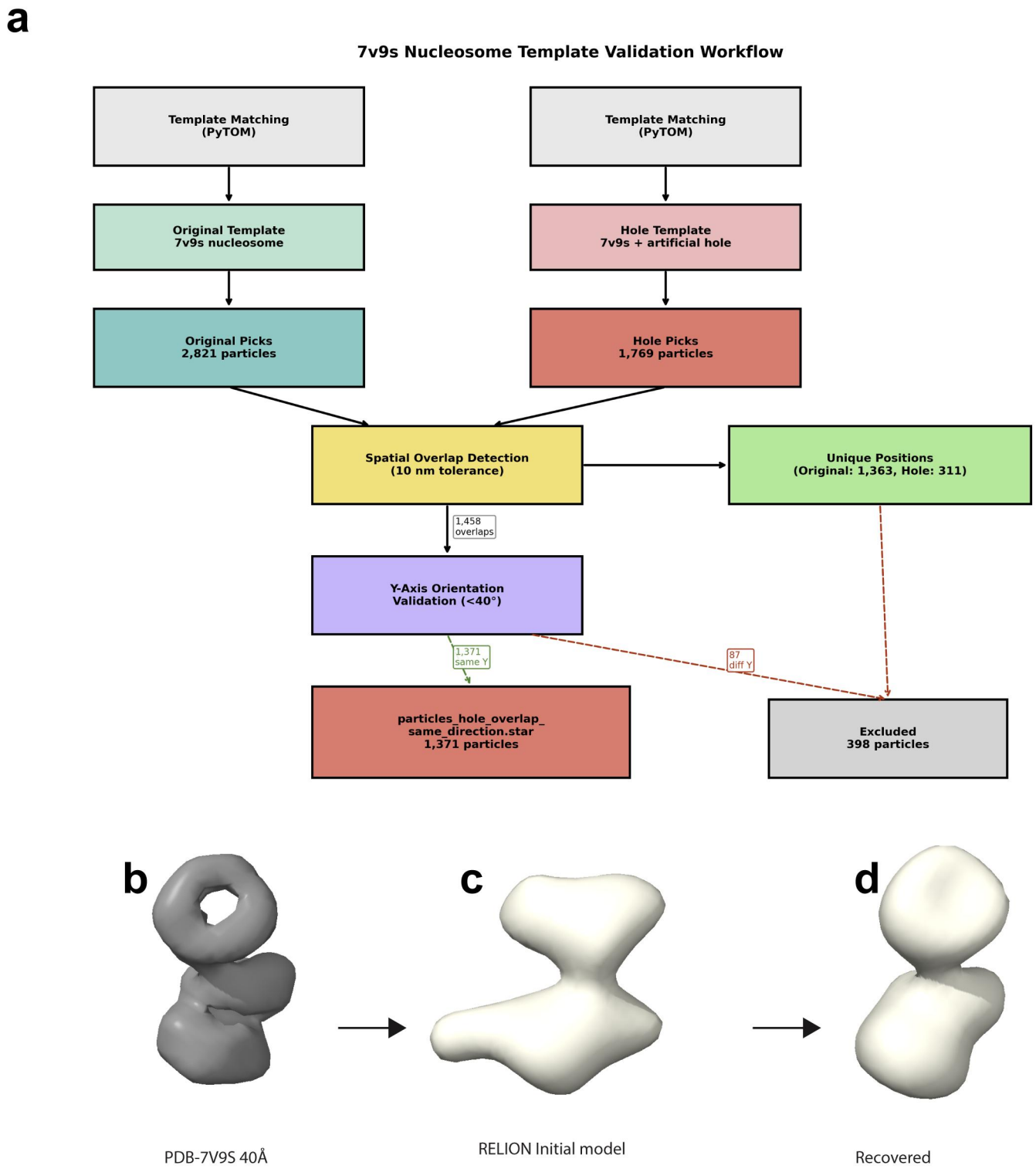



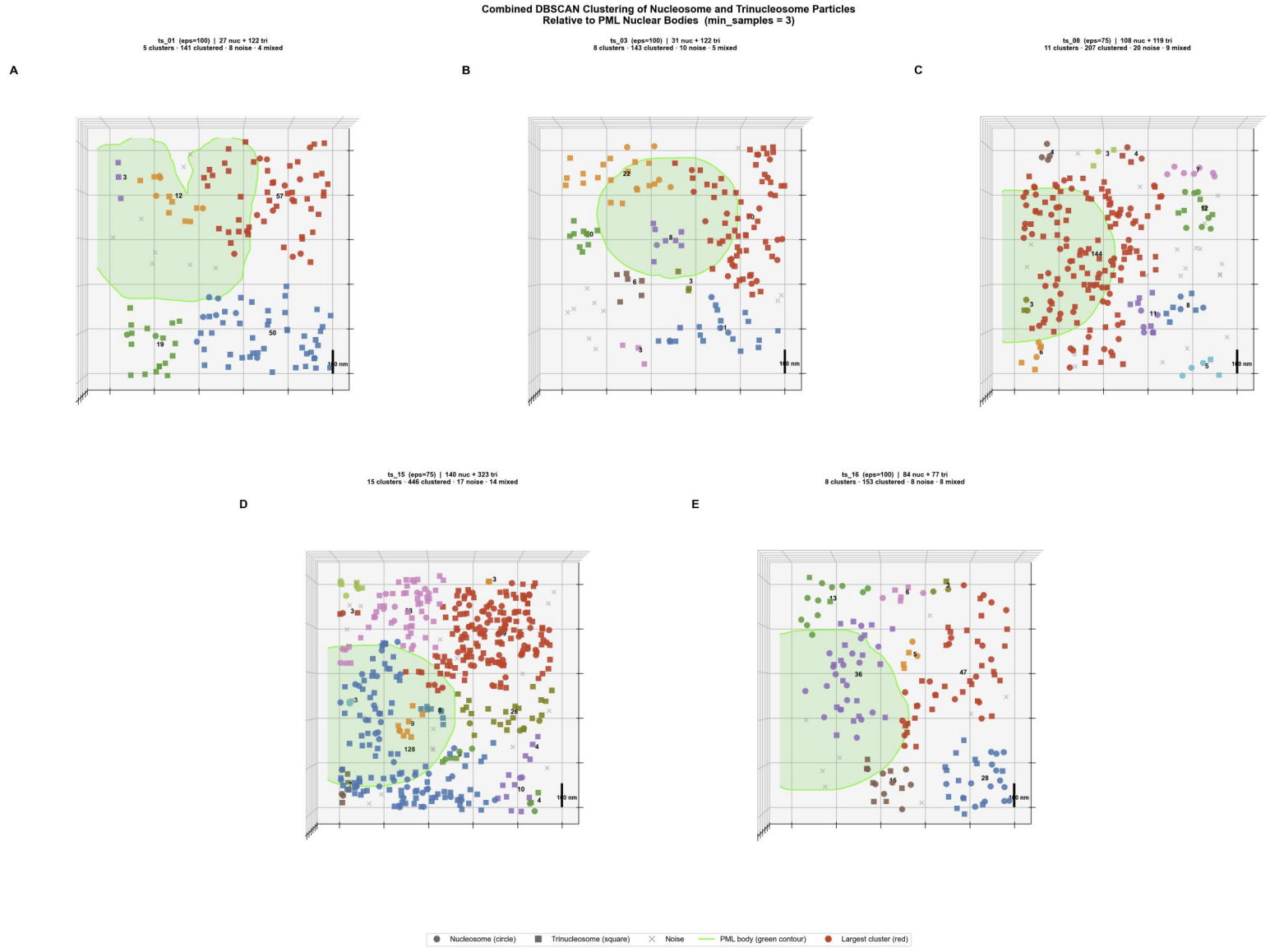

# Extended Data Fig. 5




# Extended Data Fig. 6




Extended Data Fig. 7




# Extended Data Fig. 8

## Supplementary Files

This is a list of supplementary files associated with this preprint. Click to download.

- PMLbodiesNCBv2SupplementaryInformation20261028.pdf
- Movie4.mp4
- Movie5.mp4
- Movie3.mp4
- Movie12.mp4
- Movie8.mp4
- Movie1.mp4
- Movie9.mp4
- Movie11.mp4
- Movie7.mp4
- Movie2.mp4
- Movie10.mp4
- Movie6.mp4